Dynamic Mode Decomposition applied to Solid States Quantum Mechanical Systems

Bachelor Project

Light-matter Interaction Group, Physics department,
University of Fribourg
by

Léo Mayques

April 2025

Supervisor:
Dr. Michael Schüler
Light-matter Interaction Group, Physics department, University of Fribourg

Abstract

Dynamic Mode Decomposition (DMD) is a data-driven method for the analysis of dynamical systems. Contrary to classical approaches in physics, DMD allows for an equation-free description of the system under study. One of its key features is its ability to identify dominant modes in dynamical systems. Another is that it can be used for short-range spatiotemporal forecast. This makes it relevant in areas where data gathering is difficult (e.g: quantum systems, space-based measurement).

The purpose of this Bachelor Project is to explore the application of DMD to two solid state systems: the time evolution of a simple two-band model in a semiconductor, and that of a magnon distribution in a driven system. The basics of both magnon and semiconductor theory will be laid to implement and bring in context the results obtained.

Contents

1 Introduction

The study of dynamical systems is an almost ubiquitous problem in physics. Traditionally, the analysis of such systems relies on explicit modeling via general equations (like equations of motion, conservation of energy or momentum, etc...). However, setting up governing equations can prove very difficult for some problems.
Dynamic Mode Decomposition (DMD), like other data driven methods, offers a good alternative to that classical approach. It is a purely data-driven technique, originally developed in fluid dynamics for the analysis of turbulent or chaotic flows. It is used to extract spatiotemporal coherent structures (called modes) from time-resolved data.
Since its inspection, the method has been successfully applied in areas as diverse as video processing, neuroscience and epidemiology.

In this project, we focus on the application of DMD on two different types of physical systems: the density matrix of a two-band semiconductor, and the distribution of magnons in a driven-system.

The study of solid state quantum mechanical systems has become a very important field over the last century. It has greatly improved our understanding of matter and led to the discovery of stunning phenomenon like superconduction or quantum tunneling. Since its inception, the field has gone from a purely theoretical focus to being at the forefront of many of the major technological developments taking place today. The goal of this project is to consider the applicability of DMD to reconstruct the data simulated in the framework of quantum dynamics.

First, we focus on simulating a simple 1-dimensional 2-band semiconductor. The time evolution of the system is modeled using its density matrix. The physical meaning of each elements in the density matrix is discussed and a more sophisticated version of DMD, called Hankel-processed DMD is also considered, to improve the efficiency of the basic DMD algorithm.
Data from a simulation on the evolution of a magnon distribution is also used later on to study the efficiency of the DMD algorithm.
The benefits of improving on the basic DMD algorithm using Hankel processing is considered, along with the potential costs in time-efficiency and resolution.

The following work is divided as follows: Section 2 lays de basis of DMD. It explores the theoretical foundations of DMD, its basic algorithm, possible applications, as well as some shortcomings of DMD and a few possible improvements on the basic algorithm.
Section 3 and 4 explore the physics of semiconductors and magnons, respectively. In particular, the Hamiltonian used to describe the two-band semiconductor as well as the sort of electric pulse used to induce the excitation are considered. The fundamental concept of a magnon is also introduced, along with the general idea leading to the simulation of the magnon distribution, which will be used as a dataset for the application of DMD.
Finally, the results are given in Section 5 and discussed in Section 6.

2 Dynamic Mode Decomposition

Dynamic Mode Decomposition (DMD) is a data-driven approach for analyzing the dynamics of systems evolving over time. It is data-driven in the sense that it does not require assumptions to be made on the system in the form of a specific mathematical model (e.g: equations of motion). Instead, the method extracts information on the system from the data itself. This type of approach is especially attractive in complex systems, where setting up a mathematical description can be very challenging.

DMD in its current formulation first emerged in fluid dynamics as a tool to reconstruct and analyze flow dynamics in the 2000's and was quickly applied to other domains, in an era where Big Data was becoming more widespread. Importantly, DMD was shown to be very efficient in video analysis as a tool to separate background objects from moving dynamic elements. DMD has since been applied to fields as far apart from each other as neural network modeling and epidemiology, and still remains an important tool in both video and fluid dynamics analysis.

On the theory side, DMD was shown to be related to the Koopman operator theory developed in the 1930's. This connection, in addition to giving a strong formal basis to DMD, opened the possibility to a different sort of DMD, called Extended DMD, which emerges naturally from the framework of Koopman theory.

Because of its ability to extrapolate the evolution of systems after the end of the measurements, DMD can be highly relevant in physics when extending measurements is very difficult (e.g: detections by space telescopes, evolution of multibody quantum systems). It can also be used to speed up numerical techniques for solving differential equations. These are a few of the motivations for applying DMD to quantum systems as is done in the present work. [1]

2.1 DMD: The basics and the Koopman theory

First, we explore the fundamental idea behind DMD and make a quick foray into the mathematical formalism behind DMD: Koopman theory; which was first introduced in 1931. This makes it possible to explore the relation between the two and helps us see how each sheds light on our understanding of the other.
The practical DMD algorithm, as it was developed in the 2000's and is still used today will be introduced in the following subsection.

2.1.1 DMD: the core idea

DMD is generally used in the context of dynamical systems, whose state vector $\mathbf{x}$ (the set of points describing the system) behaves as:

$$\frac{d\mathbf{x}}{dt} = \mathbf{f}(\mathbf{x}, t; \mu) \tag{2.1}$$

This is a very general formula, and a large part of physics is preoccupied with the identification and the study of the behavior of (2.1). However, there are many cases where $\mathbf{f}$, or even the relevant parameters μ cannot be identified.

In such contexts, DMD postulates a linear approximation of (2.1), in the form of a linear operator $\mathcal{A}$.

$$\frac{d\mathbf{x}}{dt} = \mathcal{A}\mathbf{x} \tag{2.2}$$

For known initial conditions $\mathbf{x}(0)$, and a square matrix $\mathcal{A}$, (2.2) forms a set of first order linear differential equations, with the well-known solutions given by

[1] The rest of the section is mostly based on the book *Dynamic Mode Decomposition*, by Kutz, L. and W. Brunton and Proctor [12], as well as the other sources listed in the References

$$\mathbf{x}(t) = \sum_{k=1}^{n} \boldsymbol{\phi}_k \exp(\omega_k t) b_k = \boldsymbol{\Phi} \exp(\boldsymbol{\Omega} t)\mathbf{b}, \tag{2.3}$$

Where $\boldsymbol{\phi}_k$ and ω_k are the eigenvectors and eigenvalues of $\mathcal{A}$, and b_k the coordinates of the initial value in the eigenvector basis.

The discrete formulation of (4.2), where the discrete counterpart of $\mathcal{A}$ is $\mathbf{A}$, is

$$\mathbf{x_i} = \mathbf{A}\mathbf{x_{i+1}} \tag{2.4}$$

In (2.4), the most straightforward way of finding $\mathbf{A}$ (at least at first sight and on paper), is to find the best linear fit:

$$\|\mathbf{x}_{i+1} - A\mathbf{x}_i\|_2 \tag{2.5}$$

We shall see later that the practical algorithm for DMD leverages Singular Value Decomposition to avoid solving (2.5) directly, which can prove very difficult for large $\mathbf{A}$.

2.1.2 Koopman theory

In simple DMD, $\mathbf{x_i}$ in (2.4) is tacitly taken as the state vectors describing the system. In practice, they are the data matrices, either built from measurements or numerical simulations and are said to lie in the so-called *state space*. In a sense, $\mathbf{x_i}$ can be seen as the result of the identify function $g(\mathbf{x_i}) = \mathbf{x_i}$. That output of that transformation is said to lie in the *observable space*

In general, however, g is under no obligation to be the identity function. For example, g can well be an infinite sum of non-linear functions.
By transforming $\mathbf{x}_i \rightarrow \mathbf{g}(\mathbf{x}_i) = g_1(x_{i,1}) + g_2(x_{i,2}) + ...$, one reintroduces nonlinearities "under the hood", by setting up a linear representation of non-linear functions.

Formally, the infinite-dimensional Koopman operator $\mathcal{K}$ acting on the function g is introduced as:

$$\mathcal{K}g(\mathbf{x}) = g(\mathbf{f}(x)) \tag{2.6}$$

And for the discrete case:

$$\mathcal{K}_t g(\mathbf{x}_i) = g(F_t(\mathbf{x}_i)) = g(\mathbf{x}_{i+1}) \tag{2.7}$$

In (2.6), taking g to be the identity leads back to (2.4). However, (2.7) is far more general, as it exists in an infinite function space. Using a finite truncation of (2.7) with non-identity functions g is called extended DMD and can be very efficient if g is properly chosen (which can be very difficult to do).

2.2 Using DMD

The use of DMD revolves around identifying the dominant modes in the data (using Singular Value Decomposition), finding the linear approximation operator $\mathbf{A}$, reconstructing the data, and identifying the proper truncation rank r to balance speed and accuracy.

2.2.1 The DMD algorithm

As we mentioned in the preceding subsection, a linear fit isn't always the most efficient way of finding $\mathbf{A}$, especially when $\mathbf{A}$ is very large. A more efficient alternative is to use the Singular Value Decomposition (SVD), which expresses any matrix as the product of three simpler matrices: one containing orthonormal columns (left singular vectors), one diagonal (singular values), and one with orthonormal rows (right singular vectors). SVD is a generalization of eigenvalue decomposition to non-square matrices.

$$\mathbf{X} = \mathbf{U}\mathbf{\Sigma}\mathbf{V}^* \tag{2.8}$$

Here, $\mathbf{U}$ and $\mathbf{V}$ are unitary matrices, and $\mathbf{\Sigma}$ is a diagonal matrix containing the singular values of $\mathbf{X}$, sorted in decreasing order. By only retaining the largest singular values in the decomposition, it is possible to generate the a low-rank approximation:

$$\mathbf{X} = \mathbf{U}\mathbf{\Sigma}\mathbf{V}^* = \begin{bmatrix}\tilde{\mathbf{U}} & \mathbf{U}_{\text{rem}}\end{bmatrix} \begin{bmatrix}\tilde{\mathbf{\Sigma}} & 0 \\ 0 & \mathbf{\Sigma}_{\text{rem}}\end{bmatrix} \begin{bmatrix}\tilde{\mathbf{V}}^* \\ \mathbf{V}^*_{\text{rem}}\end{bmatrix} \approx \tilde{\mathbf{U}}\tilde{\mathbf{\Sigma}}\tilde{\mathbf{V}}^* \tag{2.9}$$

The subscript *rem* (for *remainder*) is used to denote the part of each matrix that can be truncated depending on the rank r of the approximation. If $r = 0$, no truncation occurs, and (2.7) is the same as (2.9). There is strictly no loss in precision (however minute), but the matrix remains difficult to handle. Finding the proper r is an important practical aspect of DMD.
This leads to :

$$\mathbf{A} \approx \tilde{\mathbf{A}} = \mathbf{X}'\tilde{\mathbf{V}}\tilde{\mathbf{\Sigma}}^{-1}\tilde{\mathbf{U}}^* \tag{2.10}$$

This technique makes it possible to retain the most important modes of $\mathbf{A}$ (its eigenvectors) without explicitly computing $\mathbf{A}$.
$\mathbf{A}$ can now be eigendecomposed like:

$$\tilde{\mathbf{A}}\mathbf{W} = \mathbf{W}\mathbf{\Lambda} \tag{2.11}$$

Where the columns of $\mathbf{W}$ are the eigenvectors of $\tilde{\mathbf{A}}$, and $\mathbf{\Lambda} = \text{diag}(\lambda_1, ..., \lambda_r)$ is a diagonal matrix composed of the eigenvalues of $\tilde{\mathbf{A}}$.

$$\mathbf{\Phi} = \mathbf{X}'\tilde{\mathbf{V}}\tilde{\mathbf{\Sigma}}^{-1}\mathbf{W} \tag{2.12}$$

is then said to contain the DMD modes of $\tilde{\mathbf{A}}$, with k columns ϕ_k.

Reconstructing the data from the DMD decomposition

The DMD reconstruction of $\mathbf{x}$ then takes form (2.13), where the amplitudes and the eigenmodes are combined to recreate the dynamics.

$$\mathbf{x}(t) \approx \sum_{k=1}^{r} \phi_k e^{i\omega_k t} b_k = \mathbf{\Phi} e^{\Omega t}\boldsymbol{b} \tag{2.13}$$

where:

- $\omega_k = -i\frac{\ln(\lambda_k)}{\Delta t}$
- $\Omega = \frac{ln\Lambda}{\Delta t}$
- $\boldsymbol{b}$ is the mode amplitude

The mode amplitude can be found either by projecting $\boldsymbol{x}$ on the modes like:

$$\mathbf{b} = \Phi^{\dagger}\mathbf{x}_1, \tag{2.14}$$

Or by applying a least square fit:

$$\mathbf{b} = \arg\min_{\tilde{\mathbf{b}}\in\mathbb{C}^n} \sum_{j=1}^{m} \left\| \Phi \exp(\Omega t_j)\tilde{\mathbf{b}} - \mathbf{x}_j \right\|^2, \tag{2.15}$$

Both approaches can be useful in different settings. In (2.14), the amplitude is found using the initial conditions (which can be a problem if some modes are completely absent from the initial condition). (2.15) tries to obtain b by minimizing the error via a linear least square.

2.2.2 The DMD algorithm applied to video

An interesting feature arising from (2.13), is that different frequencies ω_k correspond to different spatiotemporal frequencies in the system. For example, in reconstructing videos, different frequencies correspond to sets of pixels evolving at different speeds. This can be very useful to distinguish background from foreground elements. The background elements are often associated with so-called "stationary" modes of the system, with very small frequencies ($\omega_k \approx 0$) and associated eigenvalues $\lambda_k \approx 1$, while the foreground elements change over time and so have higher frequencies.

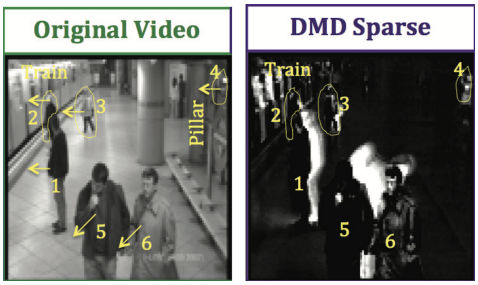

Figure 1: On the image on the right, only high frequency modes are reconstructed (i.e: taken into account in the sum in (2.13)), leading to an effective removal of the static ($\omega_k \approx 0$) background. (Image adapted from [12])

2.3 Tweaking DMD

Many flavors of the DMD algorithm have been developed over the years to better fit specific problems and solve some issues inherent to the default algorithm. For example, translations and rotations can be impossible to represent using basic DMD. This is the case for standing waves (translational behavior) that aren't picked up by DMD.
Transient behaviors were also found to pose serious challenges to DMD representation. Short lived effects are usually associated with high frequencies, but might be associated with very low amplitudes (if absent from the initial conditions). This leads to DMD missing short lived behaviors, even though they might have very strong effects on the system.

2.3.1 Multiresolution DMD

A well-known technique for detecting transient phenomena is called Multiresolution DMD. The key idea behind it is to iteratively split the data matrices into shorter time matrices to evaluate the behavior of the system over shorter time spans.
To prevent large scale modes from effectively drowning short time scales behaviors, the algorithm iteratively removes the slowest modes as it zooms in to the matrices.

$$\mathbf{x}_{\text{mrDMD}}(t) = \sum_{k=1}^{p} b_k(0)\boldsymbol{\phi}_k \exp(\omega_k t) + \sum_{k=p+1}^{m} b_k(0)\boldsymbol{\phi}_k \exp(\omega_k t) \tag{2.16}$$

In (2.14), the slow and fast modes are represented by the left-hand and right-hand side respectively. After this step, it becomes possible to split the second sum in (2.16) into two equally-sized sub-matrices. These two steps are performed iteratively until the desired timescale is reached.

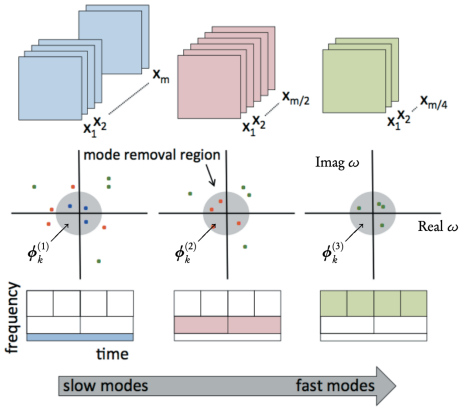

Figure 2: At each step, the lowest frequency modes are first removed from the matrix, which is then split in two. (Image adapted from [12])

The iterative nature of this algorithm makes it potentially very inefficient. However, since only the lowest frequency modes have to be effectively computed at each step, it is possible to use truncation aggressively to lower the computational load.

2.3.2 Hankel "rematrixiation"

Another way to identify transient and translational behaviors in the system is to perform so-called *Hankel preprocessing* on the $\mathbf{x}_i$ and $\mathbf{x_{i+1}}$ matrices. This technique is also called the *shift-stack* method and has the advantage of being very simple to implement. A *shift-stack* matrix transformation is of the form:

$$\begin{bmatrix} x_1 & x_2 & \cdots & x_m \end{bmatrix} \rightarrow \begin{bmatrix} x_1 & x_2 & \cdots & x_{m-1} \\ x_2 & x_3 & \cdots & x_m \end{bmatrix} \tag{2.17}$$

or more generally:

$$\begin{bmatrix} x_1 & x_2 & \cdots & x_m \end{bmatrix} \rightarrow \begin{bmatrix} x_1 & x_2 & \cdots & x_{m-s} \\ ... & & & \\ x_s & x_3 & \cdots & x_m \end{bmatrix} \tag{2.18}$$

This approach essentially increases the time resolution of the $\mathbf{x}_i$ and $\mathbf{x_{i+1}}$ matrices. This is very handy to implement, as the transformation is very easily done, and the basic DMD algorithm can then be applied to the matrices without any changes.
It should be noted, however, that the transformation has the major drawback of time-shortening the matrices in proportion to the desired increase in time-resolution.

2.3.3 Dealing with noise

In the present work, we only used noise-free synthetic data. None-the-less, DMD is often applied on real-world data, in which noise must be expected. Consequently, we list here a few of the techniques that can be used to reduce or remove noise in the context of DMD.

Optimal truncation

The first and most straight-forward way of dealing with noise is truncation of the SVD matrix. The choice of the truncation rank r of the SVD is a question often posed in DMD implementation and often involves ad hoc approaches depending on the setup.
However, in the case of a given $n \times m$ data matrix $\mathbf{Y}$, containing a signal $\mathbf{X}$ and some noise $\mathbf{X}'$ matrix composed of independently distributed gaussian entries with unit standard deviation and zero mean:

$$\mathbf{Y} = \mathbf{X} + \eta \mathbf{X}' \tag{2.19}$$

The optimal truncation threshold τ is given by

$$\tau = \sqrt{n\eta} \quad \left(2\left(\frac{m}{n} + 1\right) + \frac{8\frac{m}{n}}{\left(\frac{m}{n} + 1\right) + \left(\frac{m}{n}^2 + 14\frac{m}{n} + 1\right)^{1/2}} \right)^{1/2} \tag{2.20}$$

Of course, the noise is rarely known and must be estimated.

Backward and forward transformation

Performing DMD in the reverse order on $\mathbf{x}_2$ and $\mathbf{x}_1$ yields the reverse transformation, $\mathbf{A}^{back}$, which on a noise free measurement matrix $\mathbf{A_x}$ should respect:

$$\mathbf{A_x} = \left(\mathbf{A_x}^{back} \right)^{-1} \tag{2.21}$$

In the case of a noisy matrix $\mathbf{A}_y$, it can be shown that:

$$\mathbf{A_x} \approx \left(\mathbf{A_y} (\mathbf{A_y}^{back})^{-1} \right)^{1/2} \tag{2.22}$$

(2.22) is easily performed on noisy matrices and can lead to useful increases in precision.

3 The band model

This section introduces the relevant concepts leading up to the two-band model. It first presents the general concept of semiconductors, the geometry of crystals, the behavior of electrons in periodic potentials, and finally leads to the density matrix and the dipole moment [2].

3.1 Semiconductors

Semiconductors have become ubiquitous in the modern world. They underpin most of the technological developments of the last 50 years. Modern semiconductor physics is a field as wide as the types of materials it describes and still an expanding area of research.
In its entry on semiconductors, Wikipedia describes them as "materials with electrical conductivity between that of a conductor and an insulator". Even though this is the definition most commonly retained, it is interesting to note that the reason for their amazing usefulness springs from that their conductivity can be dynamically *tuned*, by submitting them to a chosen dynamic voltage. This is this "dynamical tunability" that makes semiconductors perfectly suited in the design of logic circuits, which are at the basis of all modern electronics.

The simplest type of semiconductors, to which most of the semiconducting materials used today still belong, are crystal semiconductors. They form regular networks, called Bravais lattices.
A very simple example of a Bravais lattice with a single type of element is silicon (Si) crystals, actually formed by two superposed so-called face centered cubic (fcc) Bravais lattices of silicon.

Binary compounds form another common type of semiconducting crystals. For example, Galium Arsenide (GaAs) follows the so-called Zinc-blende structure, wich unlike the diamond structure of silicon crystal is formed of one Ga atoms lattice, while the other is formed of As atoms.

Many elements can form semiconducting crystals, either alone (like Si), or compounded with other elements (like GaAs). Some groups in the periodic table are more auspicious to creating binary compounds, based on opposed electro-negativity with other groups (which lets them associate easily).
The electro-negativity of the two different compounds plays an important role in the band structure of the resulting semiconducting crystal (the concept of bands is fundamental in semiconductor physics and we will investigate it closely in the coming subsections). A good example are Group III and Group IV elements which easily form semiconducting compounds. Since the Goup IV is more electronegative than the Group III, the higher the polarity differences between the two compounds, the greater the polarization within the crystal and the greater the overall ionization and width of the band gaps.
The Group II and Group V compounds follow the same rule and tend to generate even more ionized semiconductors.

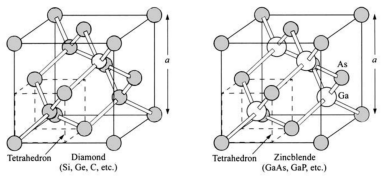

Figure 3: Two types of crystal structures: Diamond and Zincblende. Both are tetrahedron structures, meaning each atom has 4 closest neighbours. The atom is then said to be four-fold coordinated. The parameter a in the image is the crystal parameter, usually in the angstrom range. For example, $a_{\mathrm{Si}} = 543.10$ pm. (Image adapted from [7])

Many other types of semiconductors have been investigated over the years. Some, like layered semiconductors (which behave almost like non-interacting 2D semiconductors) exploit the microscopic geometry of the materials to influence their semiconducting properties.
Others, like organic compounds, make use of the great flexibility of carbon chemistry to enable the

[2] For more details on the material and derivations of section 3, see ref [1] to [8]

design of new, complex semiconductors. These exotic materials are completely out of the scope of this project and we only mention them here as a curiosity.

3.2 Crystals

Matter at the atomic scale follows the laws of quantum mechanics. In order to use our knowledge of these laws, and leverage tools like the Schrödinger equation, or even classical ones like Maxwell's laws, we first need to understand the structure and the basic geometry of the world we are exploring: That of crystals.

3.2.1 Bravais lattice

A Bravais lattice is the mathematical tool used to describe the periodicity of crystals. In 3 dimensional space, it is formally defined as the set of vectors $\mathbf{R}$ that are of the form:

$$\mathbf{R} = n_1\mathbf{a}_1 + n_2\mathbf{a}_2 + n_3\mathbf{a}_3, \quad n_i \in \mathbb{Z} \tag{3.1}$$

With $\mathbf{a}_1$, $\mathbf{a}_2$, $\mathbf{a}_3$ linearly independent vectors in $\mathbb{R}^3$. A more intuitive way of seeing (2.1) is to say that "the world seen from any node in the lattice is exactly the same as seen from any other node". This reflects the translational symmetry of crystals.

3.2.2 Crystal basis and Wigner-Seitz

In most simple crystals, like the simple cubic Bravais lattice, the periodicity of the crystal is visible at first sight: each point of the Bravais lattice is occupied by a single atoms. In these cases, the need for a basis isn't apparent, as the basis reduces trivially to a single atom. In more complicated geometries, the crystal's periodicity doesn't exist when considering individual atoms only. Some set of atoms must then be "packaged" together to allow the periodicity to become visible. Once the proper "package" is found, the crystal can be split in a periodic repetition of such "packages"(called the *basis* of the lattice). Each of these basis can then provide some anchor point for building the emerging Bravais lattice.

The volume around each lattice point that is closer to it than to any other point in the lattice is called the Wigner-Seitz cell.

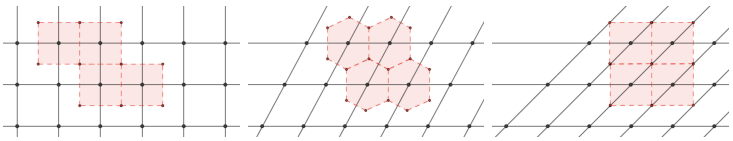

Figure 4: The Wigner-Seitz Cell for a few set of 2D Bravais lattices. Each of the Bravais lattice can be seen to have its own set of primitive lattice vectors (so called to avoid confusion with the crystal basis). (Image adapted from [6])

3.2.3 Reciprocal Space and the Brillouin zone

The quantum description of particles inside the crystal will be in the form of wave equations. Thus it is relevant to consider the Fourier Transform of the primitive lattice vectors and of the Wigner-Seitz cell.
The Reciprocal space is the name given to the Fourier transform of the real crystal space. Its primitive lattice vectors are given by:

$$\mathbf{b}_1 = 2\pi\frac{\mathbf{a}_2 \times \mathbf{a}_3}{\mathbf{a}_1 \cdot (\mathbf{a}_2 \times \mathbf{a}_3)} \quad , \quad \mathbf{b}_2 = 2\pi\frac{\mathbf{a}_3 \times \mathbf{a}_1}{\mathbf{a}_1 \cdot (\mathbf{a}_2 \times \mathbf{a}_3)} \quad , \quad \mathbf{b}_3 = 2\pi\frac{\mathbf{a}_1 \times \mathbf{a}_2}{\mathbf{a}_1 \cdot (\mathbf{a}_2 \times \mathbf{a}_3)} \tag{3.2}$$

The reciprocal space is crucial to the behavior of electrons in crystals, as it is essentially the momentum space where they live.
The Brillouin zone is the equivalent of the Wigner-Seitz cell in the reciprocal space. In the development of the theory, it will play a key role as the building block of the momentum space.

3.3 Band structure theory: electrons in a solid

Band structure theory naturally emerges from the quantum description of atoms and their periodic arrangement in crystals.
In the following, we explore the basic formulation of quantum physics for a single atom, before inserting it in the constraints of crystalline geometry already mentioned above.

3.3.1 An atomic electron in an electric field

Photons are known to be able to excite electrons in atoms if they have the proper energy level. The energy they bring can lead to either excitation or straight-down ionization, if it is sufficient to remove the electron from the atom altogether. In the following, we consider a laser pulse and approximate it classically by an electric field that influences the electron.

As an electron follows quantum dynamics, it must respect the Schrödinger equation. The general form of the Schrödinger equation for a single electron in an atom is:

$$i\hbar\frac{\partial\psi(\mathbf{r},t)}{\partial t} = \left[-\frac{\hbar^2}{2m}\nabla^2 + V_0(\mathbf{r})\right]\psi(\mathbf{r},t) \tag{3.3}$$

Where $\psi(\mathbf{r},t)$ is the wavefunction of the electron, $V_0(\mathbf{r}) = -\frac{e^2}{r}$ is the Coulomb potential due to the nucleus (assuming a hydrogen-like atom), and the Hamiltonian is given by $H_0 = -\frac{\hbar^2}{2m}\nabla^2 + V_0(\mathbf{r})$.

When the atom is placed in an electric field $\mathbf{E}(t)$, (2.3) takes in an additional term and becomes:

$$i\hbar\frac{\partial\psi(\mathbf{r},t)}{\partial t} = \left[-\frac{\hbar^2}{2m}\nabla^2 + V_0(\mathbf{r}) - e\mathbf{r}\cdot\mathbf{E}(t)\right]\psi(\mathbf{r},t) \tag{3.4}$$

Where $e\mathbf{r} = \mathbf{d}$ is the electric dipole moment. This corresponds to the effect of the time-varying electric field generated by the light on the Hamiltonian.

3.3.2 Bloch's theorem

The Bloch Theorem states that in a periodic potential, the solutions of the Schrödinger equation are plane waves containing periodic functions $\mathbf{u}(t)$ of the same periodicity as the crystal, which is expressed as:
$V_0(\mathbf{r}) = V_0(\mathbf{r}+\mathbf{R}_n)$. Where $\mathbf{R}_n = \sum_i n_i\mathbf{a}_i$ is a integer linear composition of the Bravais lattice vectors. The Bloch theorem is given by:

$$\psi(\mathbf{k},\mathbf{r}) = e^{i\mathbf{k}\cdot\mathbf{r}}u(\mathbf{k},\mathbf{r}) \tag{3.5}$$

In the approach generally accepted, the periodic potential is assumed to be much more potent than other effects, like the electric field. These effects can later be approximated as perturbations on the periodic potential model. Consequently, (3.5) is inserted in (3.3). This leads to :

$$-\frac{\hbar^2}{2m}\nabla^2\psi(\mathbf{k},\mathbf{r}) = -\frac{\hbar^2}{2m}e^{i\mathbf{k}\cdot\mathbf{r}}\left(\nabla^2 u(\mathbf{k},\mathbf{r}) + 2i\mathbf{k}\cdot\nabla u(\mathbf{k},\mathbf{r}) - k^2 u(\mathbf{k},\mathbf{r})\right) \tag{3.6}$$

The full equation becomes:

$$\left(-\frac{\hbar^2}{2m}(\nabla + i\mathbf{k})^2 + V_0(\mathbf{r})\right)u(\mathbf{k},\mathbf{r}) = E(\mathbf{k})\,u(\mathbf{k},\mathbf{r}) \tag{3.7}$$

Equation (3.7) is not easy to solve in general. In particular, it depends not only on the position, but also on the wavenumber $\mathbf{k}$. Several different approximation methods can be used to find or approximate its solutions. They include the tight-binding model, the kp model, and the pseudo-potential method. The most general is perhaps the tight-binding approach, and it is the one that will be used

in the following subsection.

3.3.3 The tight-binding approximation

The tight-binding approach assumes the electrons in the crystal to remain very close their atoms. This assumption generally leads to ignoring interaction of electrons with orbitals of atoms that are not their direct neighbors.
The model uses orbitals $|\phi_n\rangle$, localized at each lattice point n to compute the Bloch wave functions for a given crystal. In the following, we only investigate the 1-dimensional case.

$$|\psi_k\rangle = \sum_n e^{iknna}|\phi_n\rangle \tag{3.8}$$

Applying the Hamiltonian operator to (3.8) makes it possible to find the ground state via the variational method (the variational method states that the trial function can only lead to a ground state higher or equal to that of the true ground state).

$$\hat{H}|\psi\rangle = \sum_n e^{iknna}\hat{H}|\phi_n\rangle \tag{3.9}$$

$$\langle\psi|\hat{H}|\psi\rangle = \sum_{n,m} e^{ik(n-m)a}\langle\phi_m|\hat{H}|\phi_n\rangle = E_{nk}\langle\psi|\psi\rangle \tag{3.10}$$

Next, we only consider (3.10) applied to a simple 1D chain of atoms. The interaction with the second-closest orbitals and further are neglected. The electron can only hop to its closest neigbour on the right or on the left. For a simple cubic crystal, this gives the total energy at one lattice point (also called the band energy, because it is the same at all lattice points):

$$E_{nk} = \mathbf{H}_{n,n} + e^{ika}\mathbf{H}_{n,n+1} + e^{-ika}\mathbf{H}_{n,n-1} \tag{3.11}$$

Where $\mathbf{H}_{n,m} = \left\langle \phi_n \middle| \hat{H} \middle| \phi_m \right\rangle$. $J := \mathbf{H}_{n,n+1} \approx \mathbf{H}_{n,n-1}$ is introduced as a so-called "hopping parameter", encapsulating the propensity of the electron to jump to a neighboring orbital, and $\epsilon := \mathbf{H}_{n,n}$ being the energy of the electron in the present orbital.

$$E_{nk} = \epsilon - J\left(e^{ika} + e^{-ika}\right) = \epsilon - 2J\cos(ka) \tag{3.12}$$

Here we can finally note that since the crystal is periodic, the orbitals form a crystal-wide "energy layer", which is called a band.

3.4 The density operator in a 1-dimensional 2-band model

In the following, we build on the theory developed in the previous subsections to create a simple model of electrons in a 2-band semiconductor. We introduce the density operator and use it to describe the effect of an electric pulse on the coherence and population of the two bands. This approach corresponds to a very simplified version of what is done in [1]. In particular, intraband dynamics are neglected and only interband dynamics are considered. This approximation is justified by the fact that we consider a semiconductor with no electron on the conduction band at the beginning of the simulation (as opposed, for example, to a conductor where the dynamics of partially filled conduction bands play a major role).

3.4.1 The static and pulse-induced Hamiltonian

In the simple two-band model, the static Hamiltonian is simply a diagonal matrix of the form:

$$H_0(\mathbf{k}) = \begin{bmatrix} E_{VB}(\mathbf{k}) & 0 \\ 0 & E_{CB}(\mathbf{k}) \end{bmatrix} \tag{3.13}$$

In the approximation used here, the energy eigenvalues used are as follows:

$$E_{VB}(k) = 2J\cos(ka) - 2J - \frac{\Delta}{2} \tag{3.14}$$

$$E_{CB}(k) = -2J\cos(ka) + 2J + \frac{\Delta}{2} \tag{3.15}$$

Where J represents a coupling term with value of energy and Δ is the energy gap between the two bands.
Although they are reminiscent of (3.12), (3.14) and (3.15) are actually derived from the Hubbard model (see [16]), a more complete model that adds a repulsion term between electrons to the "hopping" term present in the tight-binding approach.

The pulse-induced Hamiltonian

The application of an electric current to the semiconductor modifies the static two-band Hamiltonian like so (similar to what was seen in equation (3.4)):

$$H(\mathbf{k}, t) = H_0(\mathbf{k}) + H_{int}(\mathbf{k}, t) \tag{3.16}$$

Since the interaction Hamiltonian only excites the electrons from one band to the other, it takes the following anti-diagonal form:

$$H_{int}(\mathbf{k}, t) = \mathbf{E}(t) \cdot \mathbf{D}(\mathbf{k}) = \begin{bmatrix} 0 & E(t)D(\mathbf{k}) \\ E(t)D(\mathbf{k}) & 0 \end{bmatrix} = \begin{bmatrix} 0 & V(\mathbf{k}, t) \\ V(\mathbf{k}, t) & 0 \end{bmatrix} \tag{3.17}$$

Where $\mathbf{E}(t)$ is the electric field and $D(\mathbf{k})$ the dipole electric moment.
For the purpose of this simulation and for simplicity, the dipole was taken to be equal to one.

3.4.2 The Electric Field

Two types of electric pulses are considered in the simualtion. The first is a purely gaussian curve of the form:

$$\mathbf{E}(t) = \frac{\mathbf{E_0}}{\sqrt{2\pi\sigma^2}} e^{\frac{-(t-t_0)^2}{2\sigma^2}} \tag{3.18}$$

where σ is a tuning parameter for the width of the pulse.

A slightly more realistic pulse is also considered with:

$$\mathbf{E}(t) = \frac{\mathbf{E_0}}{\sqrt{2\pi\sigma^2}} e^{\frac{-(t-t_0)^2}{2\sigma^2}} \cos(\omega(t-t_0)) \tag{3.19}$$

Where the sinusoidal term introduces an exponentially decaying oscillation inside the gaussian "envelope", which corresponds more closely to the behavior of actual laser pulses.

3.4.3 Time evolution of the density operator

The purpose of the simulation is to represent the evolution of the population of the bands over time. To do so, we introduce the density operator for two states $|1\rangle$ and $|0\rangle$

$$\hat{\rho} = |\psi\rangle\langle\psi| \tag{3.20}$$

Its general form for two states in the two-band model $|1\rangle$ and $|2\rangle$ is:

$$\rho(\mathbf{k}, t) = \begin{bmatrix} \rho_{VB}(\mathbf{k}, t) & \rho_{12}(\mathbf{k}, t) \\ \rho_{21}(\mathbf{k}, t) & \rho_{CB}(\mathbf{k}, t) \end{bmatrix} \tag{3.21}$$

It is important to note that the diagonal element correspond to the mixed state elements (no superposition), while the off-diagonal elements correspond to superposition of the two mixed states. Moreover, the density operator must be hermitian ($\rho^\dagger = \rho$), to ensure that all observables derived from it are real-valued. This implies that the off-diagonal elements of (3.20) must be the complex conjugate of one-another.

For its time evolution, (3.20) must respect the Von Neuman Equation, which is the equivalent of the Schrödinger Equation for the density matrix:

$$\frac{d}{dt}\hat{\rho}(\mathbf{k}, t) = -i\left[\hat{H}(\mathbf{k}, t), \hat{\rho}(\mathbf{k}, t)\right] \tag{3.22}$$

For clarity and simplicity, the semiconductor is taken to be in its insulator state at the beginning of the simulation, with a filled valence band and an empty conduction band (and no superposition). Simply put, this is:

$$\rho(\mathbf{k}, 0) = \begin{bmatrix} 1 & 0 \\ 0 & 0 \end{bmatrix}$$

When expanding the commutator from (3.22), defining $\Delta_{CV} := \rho_{CB} - \rho_{VB}$, the equation becomes:

$$\begin{bmatrix} \frac{d}{dt}\rho_{VB} & \frac{d}{dt}(c_1 + ic_2) \\ \frac{d}{dt}(c_1 - ic_2) & \frac{d}{dt}\rho_{CB} \end{bmatrix} = \begin{bmatrix} 2Vc_2 & -i\Delta\varepsilon(\mathbf{k})(c_1 + ic_2) - iV\Delta_{CV} \\ -i\Delta\varepsilon(\mathbf{k})(c_1 - ic_2) + iV\Delta_{CV} & -2Vc_2 \end{bmatrix} \tag{3.23}$$

Expressing the density matrix (3.21) as a 4-dimensional vector of the form : $\rho(t) = [\rho_{\mathrm{VB}}(t), \rho_{\mathrm{CB}}(t), c_1 + ic_2, c_1 - ic_2]^T$, (3.22) can be written as :

$$\frac{d}{dt}\rho(\mathbf{k}, t) = \mathbf{A}\rho(\mathbf{k}, t) = \begin{bmatrix} 0 & 0 & -iV(t) & iV(t) \\ 0 & 0 & iV(t) & -iV(t) \\ -iV(t) & iV(t) & -i\Delta\varepsilon(k) & 0 \\ iV(t) & -iV(t) & 0 & -i\Delta\varepsilon(k) \end{bmatrix} \rho(\mathbf{k}, t) \tag{3.24}$$

This is a standard differential equation that can be solved numerically using common python libraries.

Although the formalism developed to this point uses very simple assumptions (1D semiconductor, closest-neighbor-only jumps, no electron-electron interaction (Hubbard model), no explicit dependence of D on $\vec{k}$, etc...), it is important and very useful to note that the general form, in particular the dimension of (3.20), (3.22) and (3.23) remains unchanged for more complex 2-band models.

3.5 The electric dipole moment

The dipole moment of an atom is a measure of the separation between the positive (nucleus) and the negative (electron) charge [3]. It takes the form:

$$\mathbf{d} = -e\mathbf{x} \tag{3.25}$$

Since the electric dipole moment encapsulates both the proximity of the electron to the nucleus, and the electrical charge, it naturally describes "how strongly" an electric field will couple with the electrons (Indeed; both increasing the charge and the distance from the nucleus make it easier for the field to interact with them).
For orbitals in atoms, the average position of the electrons is usually located at the nucleus, leading to a zero electric dipole moment. Superposition of orbitals, however, can lead to non-zero electric dipole moments. Similarly, for the two-band model, individual bands do not have an electric dipole moment. The coherence between these bands, however, can lead to non-zero dipoles. This intuitively hints at a link between the off-diagonal elements of (3.21) and the electrical dipole moment.
These dipoles thus exist only when there is superposition (of, say, states $|f\rangle$ and $|g\rangle$), leading to a dipole moment vector:

$$\vec{M} = e\langle f|\mathbf{x}|g\rangle \tag{3.26}$$

Which in matrix form gives:

$$\mathbf{d} = -\begin{pmatrix} 0 & \mathbf{M} \\ \mathbf{M}^* & 0 \end{pmatrix} \tag{3.27}$$

It is possible to use the trace formula for the expectation value of any operator $\mathbf{A}$,

$$\langle \mathbf{A} \rangle = \mathrm{Tr}\{\rho \mathbf{A}\} \tag{3.28}$$

Inserting (3.21) and (3.27) in (3.28) leads to:

$$\langle \mathbf{d} \rangle = \mathrm{Tr}\begin{pmatrix} -\rho_{12}\mathbf{M}^* & -\rho_{VB}\mathbf{M} \\ -\rho_{CB}\mathbf{M}^* & -\rho_{21}\mathbf{M} \end{pmatrix} = -\rho_{12}\mathbf{M}^* - \rho_{21}\mathbf{M} \tag{3.29}$$

Using the fact that $\rho_{12}^* = \rho_{21}$:

$$\langle \mathbf{d} \rangle = -\mathbf{M}^*\rho_{21} - \mathbf{M}\rho_{21}^* = -2\,\mathrm{Re}[\mathbf{M}^*\rho_{21}] = -2\,\mathrm{Re}[\mathbf{M}^*\rho_{12}] \tag{3.30}$$

In component terms (assuming $\mathbf{M}$ real and constant, and neglecting the negative factor of 2), this gives:

$$d_x(\mathbf{k}, t) = M\,\mathrm{Re}[\rho_{12}(\mathbf{k}, t)] \tag{3.31}$$

[3] For more on the derivation of the electric dipole moment in a atom-light interaction, see [8]

4 Magnons

Magnetism has been known to humanity for a very long time. So long in fact that its English name goes back to the ancient Greeks, who already knew about the attracting effect magnetite (a naturally occurring mineral) could have on iron.
However, it was not before the end of the 19th century that magnetism was rigorously studied. It is around this time that Pierre Curie first described general properties such as the Curie temperature, above which ferromagnetic materials lose their spontaneous magnetization.
Later, in an important conceptual step, the mean field theory was developed by Weiss, who postulated that magnetization in solids arose from the interplay of very small magnetic domains, each with its own magnetic moment.

That description of "molecular magnetic moments" was latter justified by the discovery of the electron spin and of the atomic magnetic moment. These new conceptual tools allowed for a closer inspection of the microscopic behavior of the magnetic moment in solids. It was shown that the magnetic moment would precess under the influence of an external magnetic field giving rise to delocalized waves of magnetic moment oscillation. It is Felix Bloch who first proposed the idea of such spin-waves in the 1930's, whose quantization then gave birth to the concept of magnons. [4]

4.1 Magnetization in solids

The apparent magnetization of solids, as it appears in ferromagnetism, arises from the individual atomic magnetic moments ($\boldsymbol{\mu}$). These magnetic moments are themselves a result of the orbital ($\mathbf{L}$) and spin ($\mathbf{S}$) angular momenta generated by the electrons orbiting around the nucleus.

$$\boldsymbol{\mu} = -g\mu_B(\mathbf{L} + \mathbf{S}) \tag{4.1}$$

(In (4.1), μ_B is a constant called the Bohr magneton and g is called the spectroscopic splitting. Latter on, the total angular momentum is used, namely: $\mathbf{J} = \mathbf{L} + \mathbf{S}$.

As it is often impossible to deal directly with the astronomic number of atoms appearing at the microscopic scale, it is handy to introduce a macroscopic quantity, called the magnetization vector, defined as the volumetric average of the individual magnetic moments:

$$\mathbf{M} = \frac{1}{V}\sum_i \boldsymbol{\mu_i} \tag{4.2}$$

A magnetic moment will naturally tend to align with an outside magnetic field $\mathbf{B}$. If misaligned, the field will exert a torque onto the magnetic moment given by:

$$\boldsymbol{\tau} = \boldsymbol{\mu_i} \times \mathbf{B} \tag{4.3}$$

Also, since the moment itself is a scalar product with an angular momentum, the torque can also be expressed as :

$$\boldsymbol{\tau} = \frac{d}{dt}\mathbf{J} \tag{4.4}$$

$\mathbf{B}$ can then be redefined by $\mathbf{B} = \mu_0(\mathbf{H} + \mathbf{M})$, where $\mathbf{H}$ is the field's intensity and μ_0 the permeability of the vacuum.
This leads to the Landau-Lifshitz equation, which describes the motion of the magnetization under the influence of the outside field.

$$\frac{d\mathbf{M}}{dt} = -g\mu_B\mu_0(\mathbf{M} \times \mathbf{H}) \tag{4.5}$$

The same phenomenon is more generally described for single object (like an atom) as the Larmor precession, in which the object's magnetic moment is made to rotate around an external magnetic field.

[4] Subsection 4.1 and 4.2 are mostly based on [9]. See Chapters 1-3 for more details

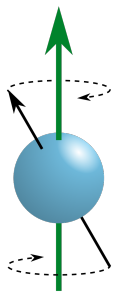

Figure 5: Larmor Precession: The magnetic moment (black arrow) rotates around the magnetic field (green arrow). (Image adapted from [9])

Projection of (4.5) in the plane perpendicular to the magnetic field yields two simple equations that lead to an expression for the precession frequency ω_0, called the resonance frequency.

4.2 Spin-waves

Although it was derived using the atomic magnetic moment, the preceding approach leads to a general, macroscopic description of the magnetization, that does not account for atomic-level interactions. One of the main shortcomings of the classical mean field model is that it does not account for lowerings of the spontaneous magnetization that occurs even well below the Curie temperature. This can be remedied by introducing spin-waves, propagating throughout the material as temperature increases, leading to disturbances in the, and an overall lowering of, the spontaneous magnetization.

When neglecting the orbital angular momentum, the exchange energy between two atoms having electrons with spin S_j, S_i and a constant in units of energy J, is written as:

$$U_{ex} = -2J\mathbf{S_i} \cdot \mathbf{S_j} \tag{4.6}$$

A simple case can be setup as a one-dimensional chain of spin, where each spin S_i only interacts with its two closest neighbors S_{i+1} and S_{i-1}.
Using 3.5 and neglecting the orbital angular momentum, the field arising in S_i can then be written as:

$$\mathbf{H}_{\text{ex}} = -\frac{2J}{g\mu_B\mu_0}\left(\mathbf{S}_{i-1} + \mathbf{S}_{i+1}\right) \tag{4.7}$$

Similar to equation (4.4), an equation of motion of motion for the spin arises when considering the effect of an outside magnetic field $\mathbf{H}$, such that the total magnetic field is $\mathbf{B}_\tau = \mu_0(\mathbf{H}_{\text{ex}} + \mathbf{H})$:

$$\frac{d\mathbf{S}_i}{dt} = -\gamma\mu_0\mathbf{S}_i \times (\mathbf{H} + \mathbf{H}_{\text{exc}}) \tag{4.8}$$

Equation (4.7) can be projected on the plane perpendicular to the direction of the field (assumed to be along $\hat{z}$). Using the identity for the projection on the x-axis of a cross product: $(\mathbf{S}i \times \mathbf{H}_{\text{ex}})^x = S_i^y H_{\text{ex}}^z - S_i^z H_{\text{ex}}^y$, and assuming that the spin is mostly parallel to the magnetic field, that is that: $S^y, S^x << S^z \approx S$,

$$\frac{dS_i^x}{dt} = \gamma\mu_0 H S_i^y + \frac{2JS}{\hbar}\left(2S_i^y - S_{i-1}^y - S_{i+1}^y\right), \tag{4.9}$$

A similar expression as (4.8) can be found for the projection on the y-axis. Importantly, both have plane wave solutions of the form $S_i^x = A_x\, e^{i(kx_i - \omega t)}$ and $S_i^y = A_y\, e^{i(kx_i - \omega t)}$, respectively, where x_i refers to the position of the ith spin in the 1D chain, ω to the angular frequency of the precession and k to the wave number. These solutions correspond to delocalized oscillation traveling across the 1D chain, called a spin-wave. Such waves can also be shown to exist more generally in 3D materials.

4.3 Magnons

The spin-waves described in the preceeding subsection occur at very small scales, and arise from spins, which are quantum objects. Consequently, a quantum description of spin-waves should be introduced. The quantization of spin-waves leads us to define spin-waves quanta: magnons.
In a 1940 paper, Holstein and Primakoff introduced the eponymous transformation that allows mapping of the spin operators to magnon operators. These magnon operators, that are no other than creator ($a_k^\dagger$) and annihilator (a_k) operators for magnons, were found to respect bosonic relations and consequently, magnons to behave like bosons.

They make it possible to express the material's Hamiltonian as the sum of a ground state energy (E_0), the independent magnon contributions and a third term, accounting for the interaction between the magnons themselves.

$$\hat{H} = E_0 + \sum_k \hbar\omega_k a_k^\dagger a_k + \hat{H}_{\text{int}} \tag{4.10}$$

This is a very general formula, with similar expressions existing for other bosons like photons or phonons.

4.3.1 Simulating magnon distributions in a driven-dissipative system

In 2022, [11] studied the dynamics of magnons in a driven system. In their theoretical setup, a radiation pulse drives the system, while a reservoir removes energy from it.
Previous research had already underlined the existence of order-disorder phase transitions in systems converging towards equilibrium. The focus of [11] was on other phase transitions arising in non-equilibrium steady-state systems. This new phase transition arose from magnons accumulating at the lowest energy level, reminiscent of the emergence of Bose-Einstein condensates.

In its approach [11] introduced a Hamiltonian not unlike (4.10), but with a second term in the summation corresponding to a second magnon branch.

$$H_0 = \sum_k \hbar\omega_k \left(\alpha_k^\dagger \alpha_k + \beta_k^\dagger \beta_k\right) \tag{4.11}$$

In [11], magnon-magnon interactions are taken to be non-dissipative. They only redistribute the energy of the interacting magnons, leading to changes in the magnon frequency distribution ($n(\omega)$). Energy and magnons are naturally allowed to dissipate inside the reservoir, and to be excited by the drive, which is assumed to be high-frequency but non-resonant.
For the simulation, the time evolution of the magnon distribution in an antiferromagnet is taken to follow from the equation of motion:

$$\frac{d}{dt} n(\mathbf{k}, t) = S[n(\mathbf{k}, t)] \tag{4.12}$$

Which describes magnon-magnon scattering inside the material.

5 Results

5.1 Setting up the semiconductor simulation

The following results were obtained using the Python programming language. The standard libraries [19], [18] and [20] where used to numerically solve differential equations, store data and display the results, respectively.

5.1.1 The band structure

Using the theory developed in section 3.3, in particular equation (3.14) and (3.15), we model the basic band structure for a few values of Δ (the band gap), and J (the coupling term).

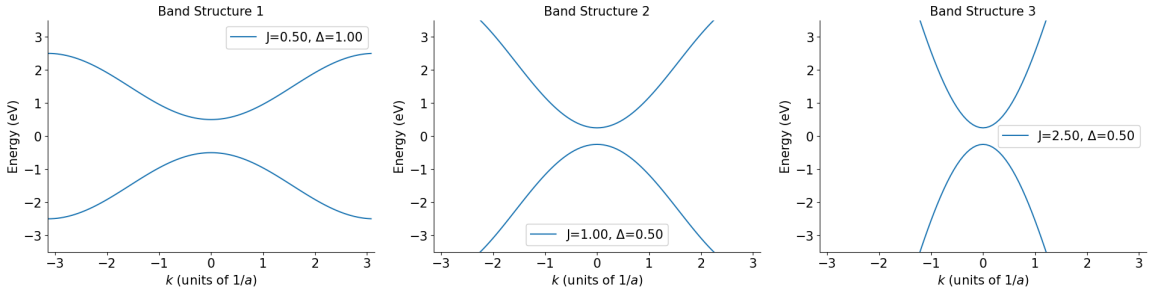

Figure 6: The band structure for three pairs of value (Δ, J), a is the crystal constant

It can be seen that Δ corresponds to the width of the band gap, while the coupling term J corresponds to the curvature of the band structure.

5.1.2 The electric pulses

Two types of pulses are used for the simulation. A simple gaussian pulse, and a more realistic "envelope" pulse, containing decaying oscillations inside a gaussian envelope.

The simple Gaussian pulse

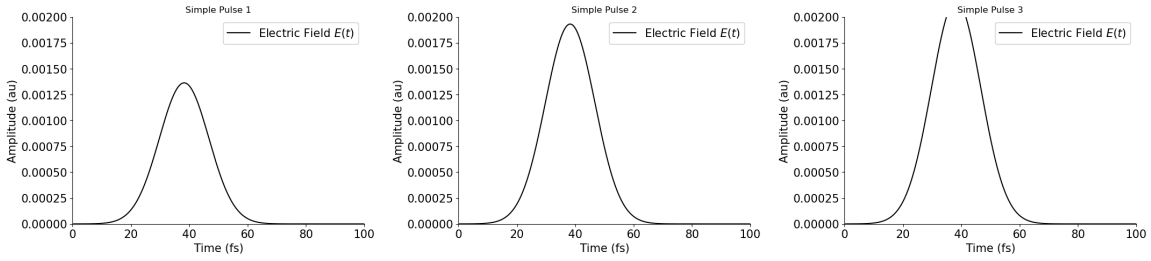

Figure 7: The simple gaussian pulse for an initial field of $E_0 = 1.2, 1.7$ and 1.9 in arbitrary units

The envelope pulse

Equation (3.19) mentioned in the theory part describes the envelope pulse : $\mathbf{E}(t) = \frac{\mathbf{E_0}}{\sqrt{2\pi\sigma^2}} e^{\frac{-(t-t_0)^2}{2\sigma^2}} \cos(\omega(t-t_0))$, with the sinusoidal term corresponding to the oscillation within the exponential envelope, already described by the gaussian above.

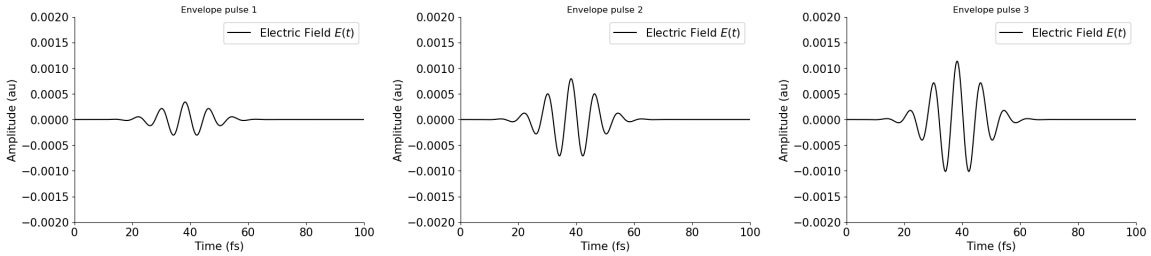

Figure 8: The envelope gaussian pulse for an initial field of $E_0 = 0.3, 0.7$ and 1.0 in arbitrary units

5.2 Effect of the pulses on the density matrix

The following shows a selection of pulse and band-structure pairs that encapsulate the general behavior of all 18 band structure and pulse pairs, following from the above. To see all 18 possible combinations, see Appendix A.

5.2.1 Simulation of the coherent, off-diagonal density matrix elements

We now use the expression for the time evolution of the density matrix obtained earlier to compute the numerical solution using the standard SciPy library. For the first part, we focus on the coherent (off-diagonal) elements of the density matrix.

Simple pulses and the superposition of the population of the bands

The following displays the effect of all three simple pulses considered above on the band structure 1. They illustrate the effect of the excitation of the coherent part of the density matrix.

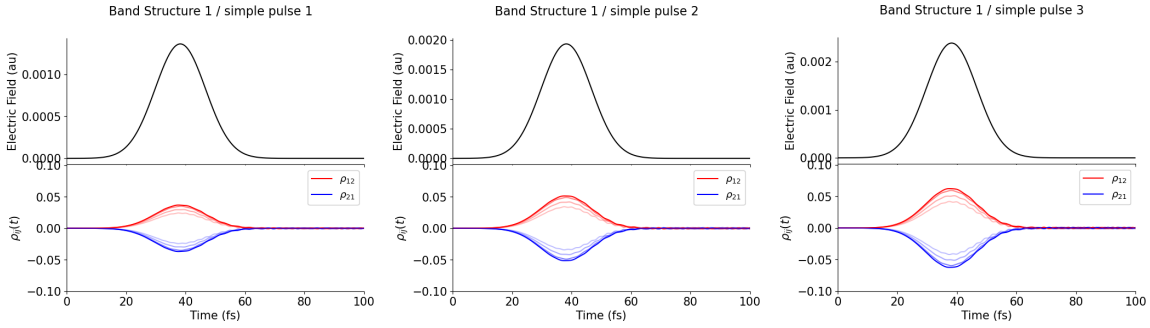

Figure 9: Effect of all three simple pulses on the first ($J = 0.5$, $\Delta = 1.0$) band structure. The different blue and red lines represent the dynamics for a few different k.

Envelope pulses and the superposition of the population of the bands

The following displays the effect the lowest power pulse on all three bands. A new behavior emerges, with the coherence remaining in a steady oscillating state, rather than disappearing with the excitation.

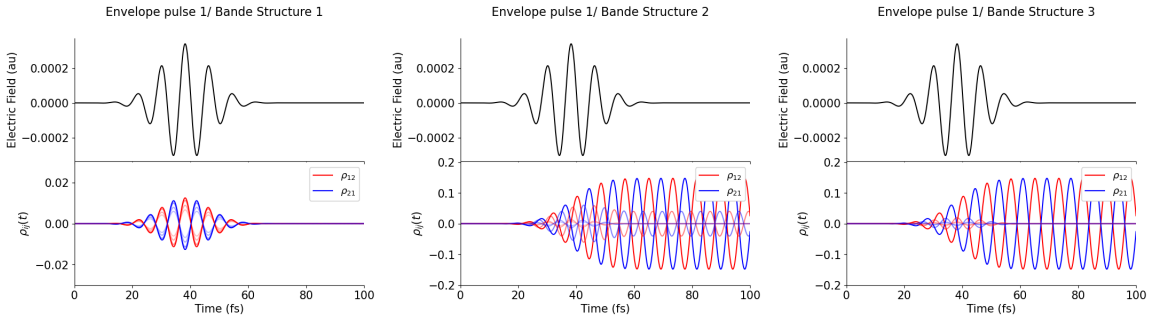

Figure 10: Effect of the envelope pulse with $E_0 = 0.3$ on all three band structures. The different blue and red lines represent the dynamics for a few different k.

5.2.2 Simulation of the valence and conduction bands populations

Like before, we use the expression for the time evolution of the density matrix to compute the numerical solution, this time of the diagonal elements of the matrix.

Simple pulses and the band populations

The following displays the effect of all three simple pulses considered above on the band structure 1. They illustrate the effect of the excitation of the population of the bands.

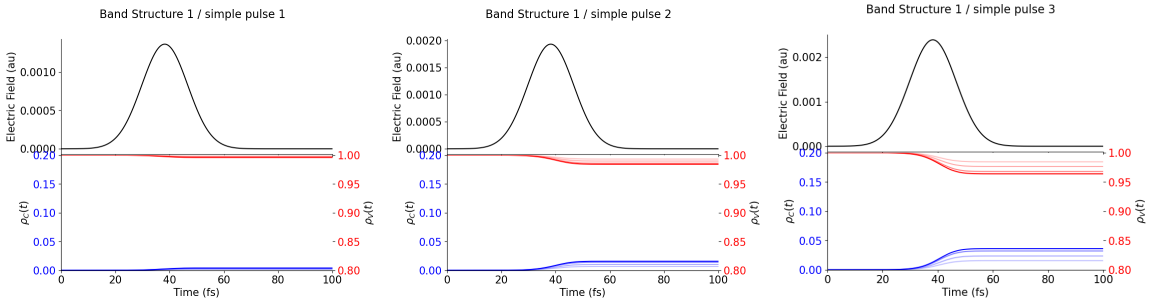

Figure 11: Effect of all three simple pulses on the first ($J = 0.5$, $\Delta = 1.0$) band structure. The different blue and red lines represent the dynamics for a few different k.

Envelope pulses and the band populations

The following displays the effect of the lowest energy envelope pulse on each of the three bands. There is a small difference with the type of excitation appearing above (see the wave-like shape of the time evolution of the populations).

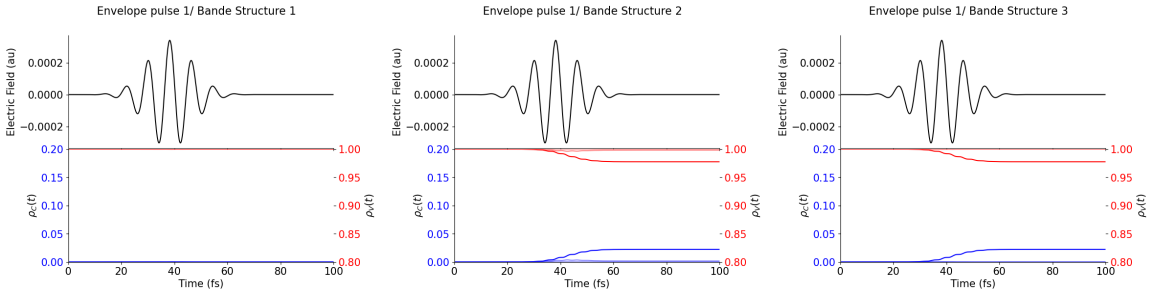

Figure 12: Effect of the envelope pulse with $E_0 = 0.3$ on all three band structures. The different blue and red lines represent the dynamics for a few different k.

5.2.3 DMD reconstruction of the off-diagonal elements of the density matrix

The PyDMD python package [21] was used in the following for both the simple DMD algorithm and the more involved Hankel-pre-processed version. This was done along a custom implementation of both versions of the algorithm.

5.2.4 Basic DMD reconstruction

In the following, the truncation rank (cutoff i) is set at 11. Eigenvalues of A are plotted on the imaginary circle.
In this first step, the simplest version of DMD is applied, for the case of the simple pulse, for the second band structure ($J = 1.0$, $\Delta = 0.5$).
Note that the singular values are always plotted in logarithmic scale.

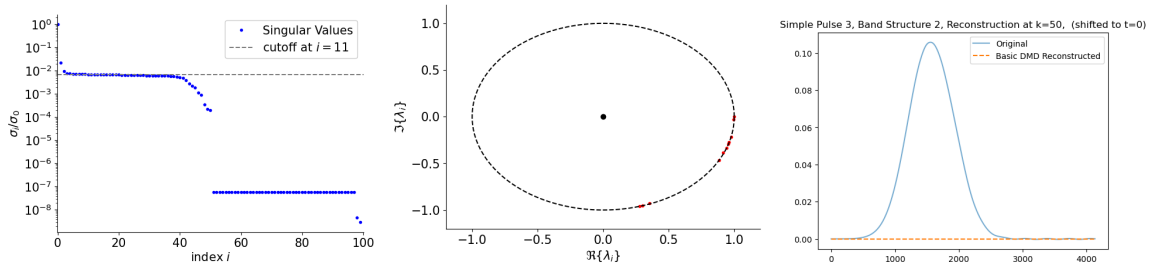

Figure 13: Result for a simple pulse excitation, $E_0 = 1.2$. For the rightmost graph: The evolution of the diagonal elements in arbitrary units (see figures 9-12). The number of time steps are plotted on the y axis.

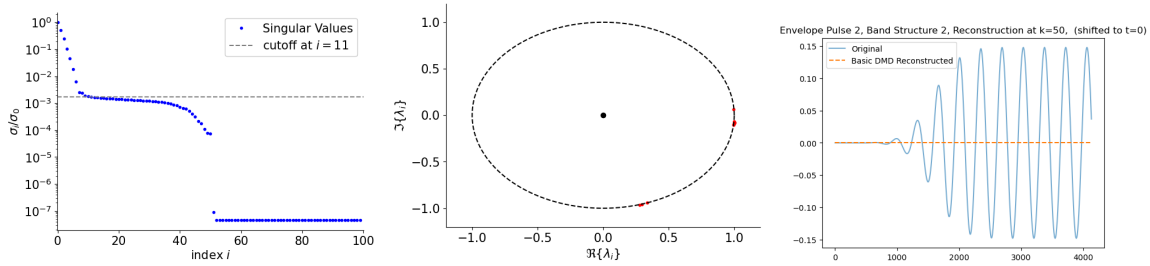

Figure 14: Result for a simple pulse excitation, $E_0 = 1.7$. For the rightmost graph: The evolution of the diagonal elements in arbitrary units (see figures 9-12). The number of time steps are plotted on the y axis.

In this first approach, the DMD reconstruction is clearly failing. The next step is to consider so-called Hankel pre-processing, to try and improve the accuracy of the reconstruction.

5.2.5 Reconstruction using Hankel pre-processing for the simple pulse case

In the following, Hankel pre-processing is used with a delay of 400, on a total time interval of 1000.

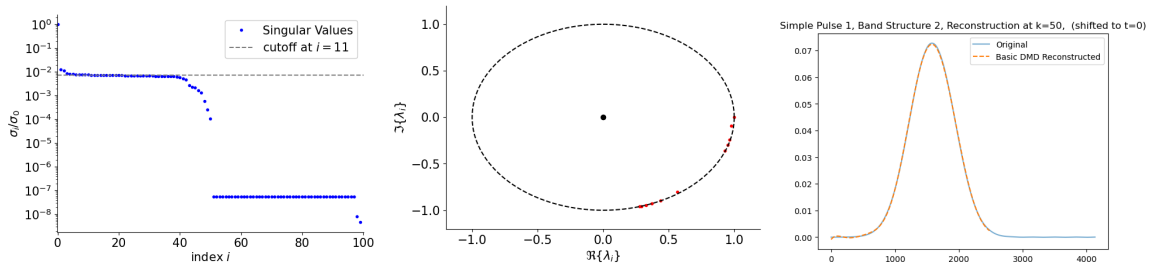

Figure 15: Result for a simple pulse excitation, modeled using Hankel pre-processing; $E_0 = 1.2$. For the rightmost graph: The evolution of the diagonal elements in arbitrary units (see figures 9-12). The number of time steps are plotted on the y axis.

5.2.6 Reconstruction using Hankel pre-processing for the envelope pulse case

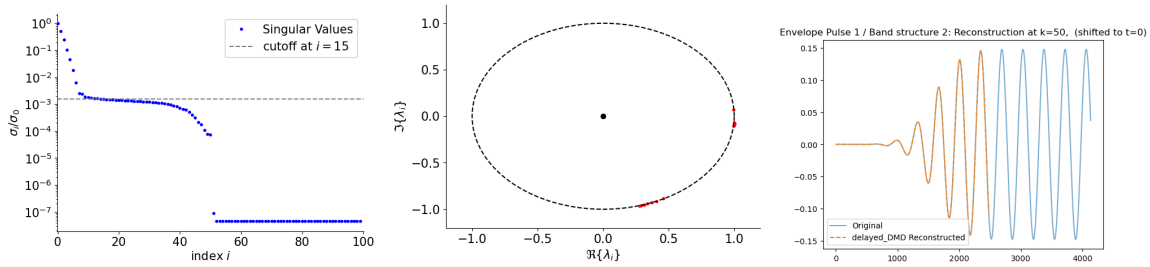

Figure 16: Result for the envelope pulse excitation, modeled using Hankel pre-processing; $E_0 = 0.3$. For the rightmost graph: The evolution of the diagonal elements in arbitrary units (see figures 9-12). The number of time steps are plotted on the y axis.

Since the agreement between the DMD reconstruction and the original data isn't as good as for the simple pulse transition, we consider different k and different truncation ranks.

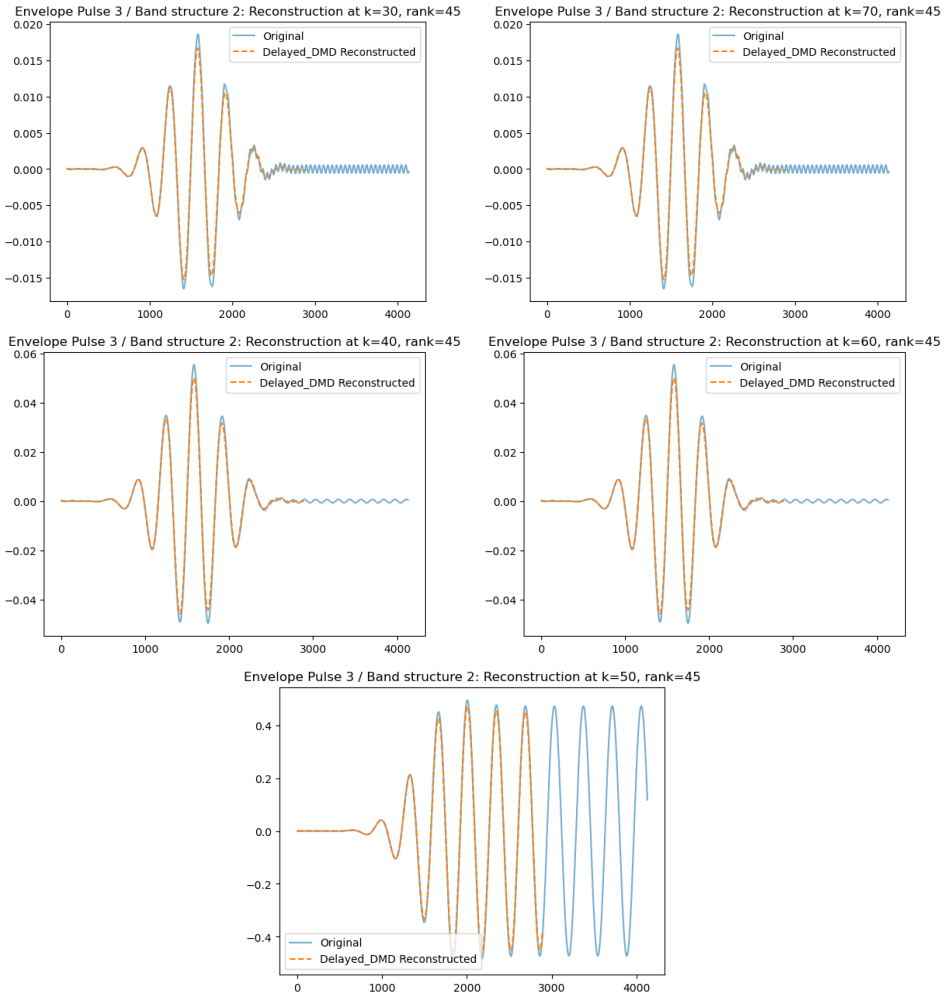

Figure 17: The amplitude of the excitation is maximal at $k = 50$ and symmetrical around that point, that is apparent above. More importantly, the precision of the DMD algorithm, although it generates an important relative error for k with small associated amplitudes, actually retains a rather good absolute accuracy, when considering the scale of the oscillation. The evolution of the diagonal elements in arbitrary units (see figures 9-12). The number of time steps are plotted on the y axis.

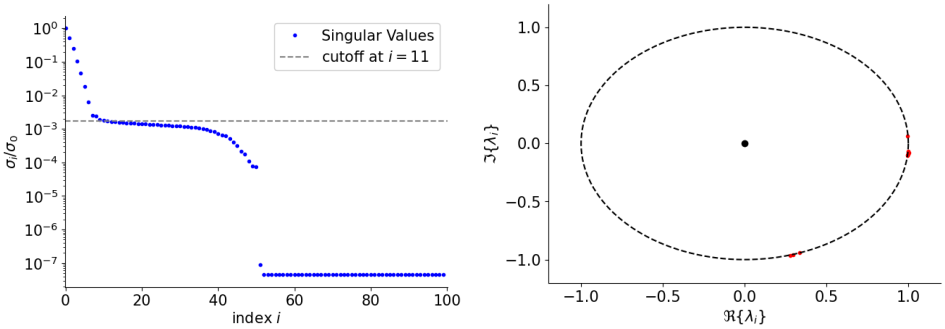

Figure 18: Plot of the singular values and projection of the eigenvalues of A on the imaginary circle

5.3 DMD reconstruction for the conduction bands

5.3.1 Basic DMD reconstruction

In the following, the truncation rank (cutoff i) is set at 11. Eigenvalues of A are plotted on the imaginary circle.
In this first step, the simplest version of DMD is applied, for the case of the simple pulse, for the second band structure ($J = 1.0$, $\Delta = 0.5$). The rightmost graphs are the evolution of the diagonal elements in arbitrary units (see figures 9-12). The number of time steps are plotted on the y axis.

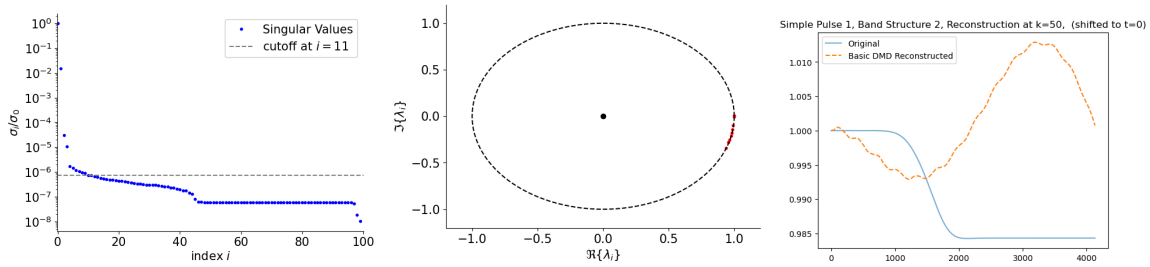

Figure 19: Result for a simple pulse excitation, $E_0 = 1.2$

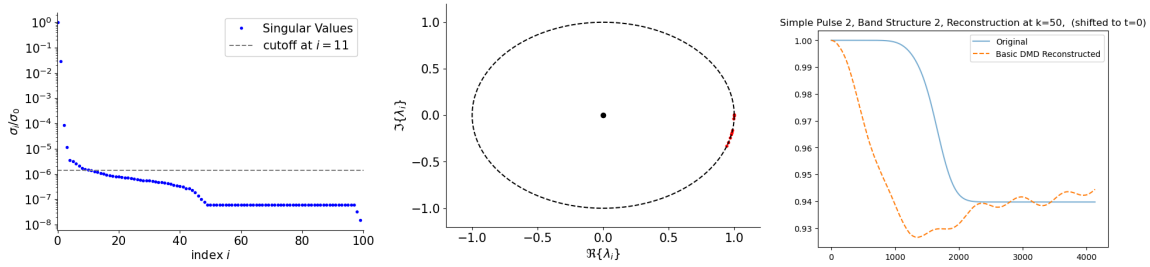

Figure 20: Result for a simple pulse excitation, $E_0 = 1.7$

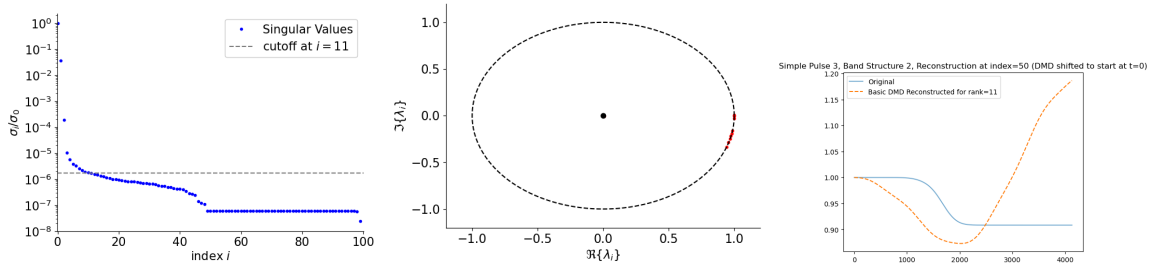

Figure 21: Result for a simple pulse excitation, $E_0 = 1.9$

As for the case of the off-diagonal elements, the DMD reconstruction is clearly failing with this first simple approach. The next step is to consider so-called Hankel pre-processing, to try and improve the accuracy of the reconstruction.

5.3.2 Reconstruction using Hankel pre-processing for the simple pulse case

In the following, Hankel pre-processing is used with a delay of 400, on a total time interval of 1000.

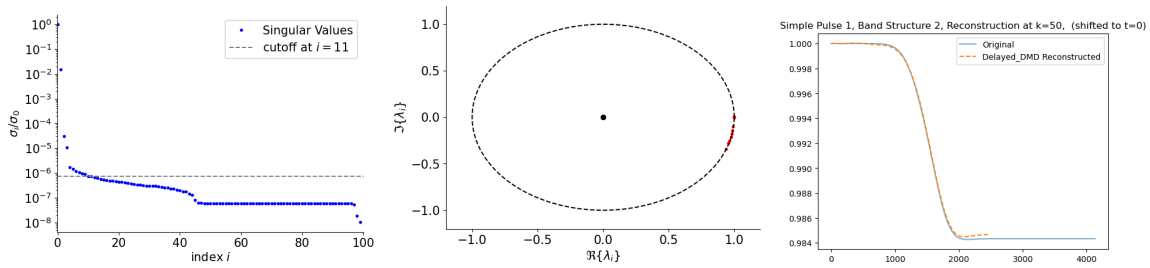

Figure 22: Result for a simple pulse excitation, modeled using Hankel pre-processing; $E_0 = 1.2$

5.3.3 Reconstruction using Hankel pre-processing for the envelope pulse case

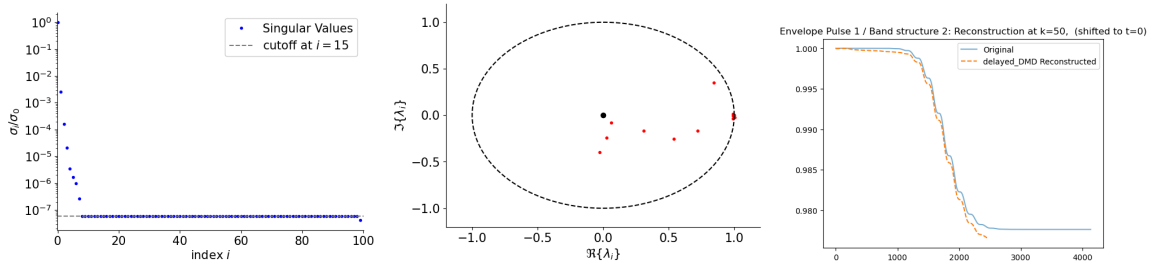

Figure 23: Result for the envelope pulse excitation, modeled using Hankel pre-processing; $E_0 = 0.3$

Since the agreement between the DMD reconstruction and the original data isn't as good as for the simple pulse transition, we consider different k and different truncation ranks.

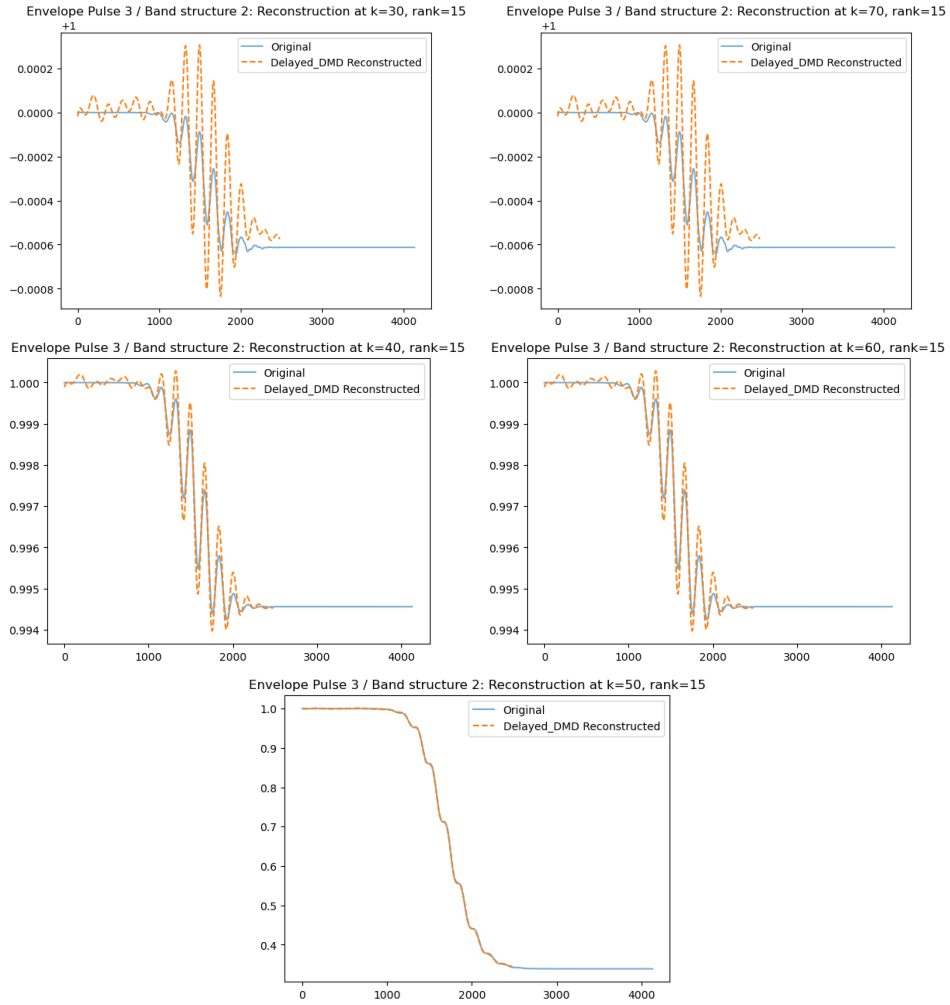

Figure 24: The amplitude of the excitation is maximal at $k = 50$ and symmetrical around that point, that is apparent above. More importantly, the precision of the DMD algorithm, although it generates an important relative error for k with small associated amplitudes, actually retains a rather good absolute accuracy, when considering the scale of the oscillation.

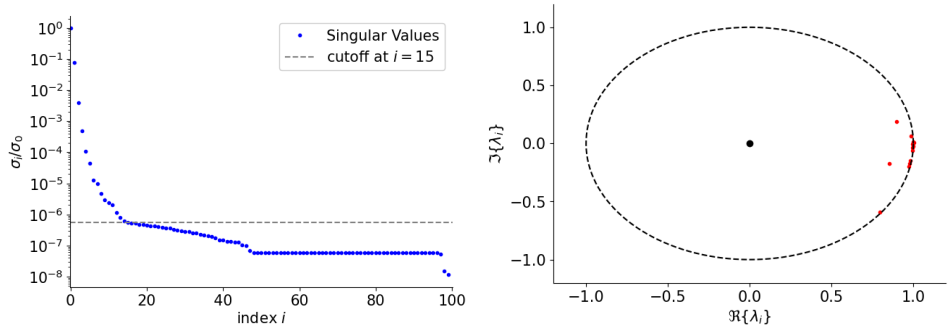

Figure 25: Plot of the singular values and projection of the eigenvalues of A on the imaginary circle

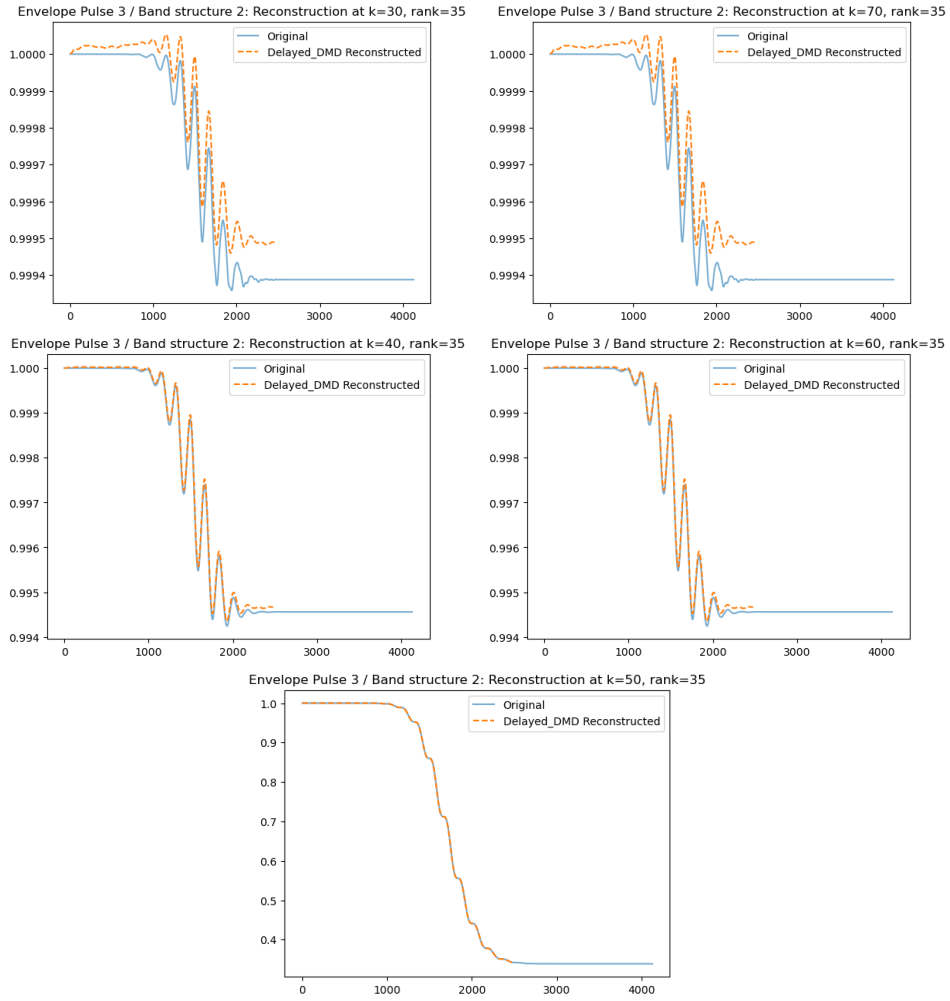

Figure 26: The amplitude of the excitation is maximal at $k = 50$ and symmetrical around that point, that is apparent above. More importantly, the precision of the DMD algorithm, although it generates an important relative error for k with small associated amplitudes, actually retains a rather good absolute accuracy, when considering the scale of the oscillation.

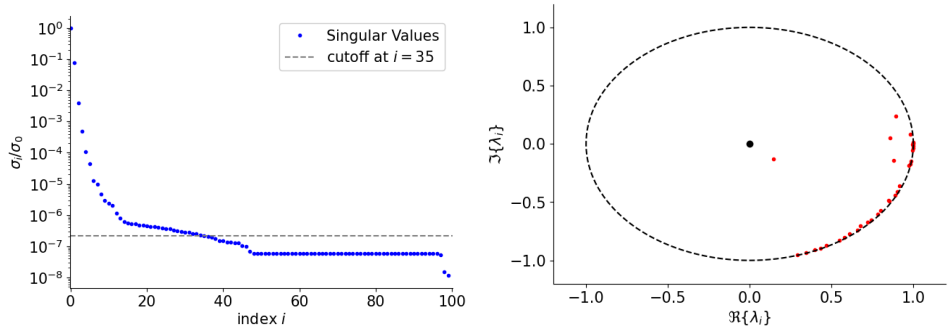

Figure 27: Plot of the singular values and projection of the eigenvalues of A on the imaginary circle

5.4 DMD error as a function of the time delay in Hankel preprocessing

Above, it has been seen that Hankel pre-processing can remarkably increase the precision of the DMD algorithm. In most cases, the introduced time delay can even be shown to have a much greater impact on the quality of the output than the truncation rank. The following graphs make it possible to explore clearly that relationship.

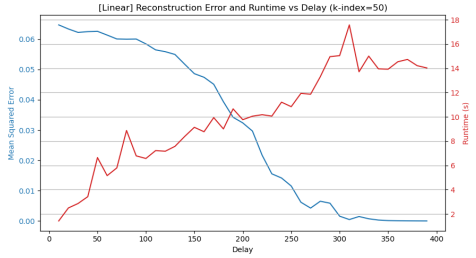

Figure 28: Error and processing time as a function of the delay introduced in Hankel pre-processing.

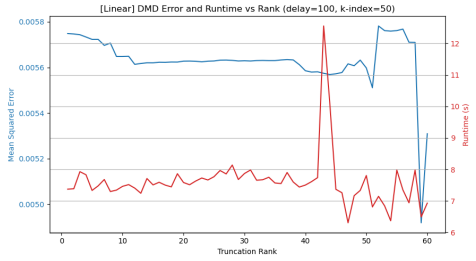

Figure 29: Error as a function of the truncation rank introduced in Hankel pre-processing.

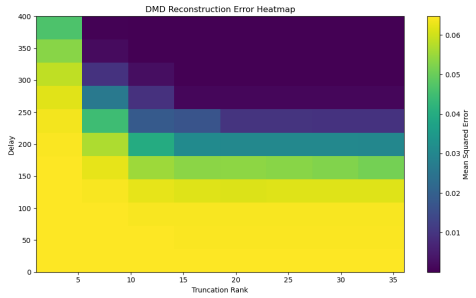

Figure 30: 2D heatmap of the error as a function of the delay and truncation rank

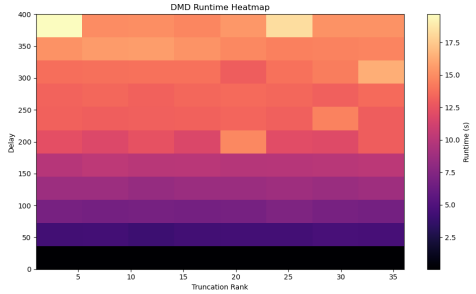

Figure 31: 2D heatmap of the processing time as a function of the delay and truncation rank

5.5 DMD reconstruction of the magnon simulation

The simulation is ran based on a momentum-resolved version of equation (4.12) from [11].
The data from the simulation is a 2-dimensional time-evolution of the magnon density. It is recast to fit the structure (1D time-evolution) of the DMD algorithm used earlier, which is then directly applied it. Two simulations are considered: the first with a total duration of 100 time steps. The second of 10'000 time steps.

5.5.1 First reconstruction with duration=100

The first simulation with duration of 100 time steps has a momentum space resolution of 128x128 pixels.

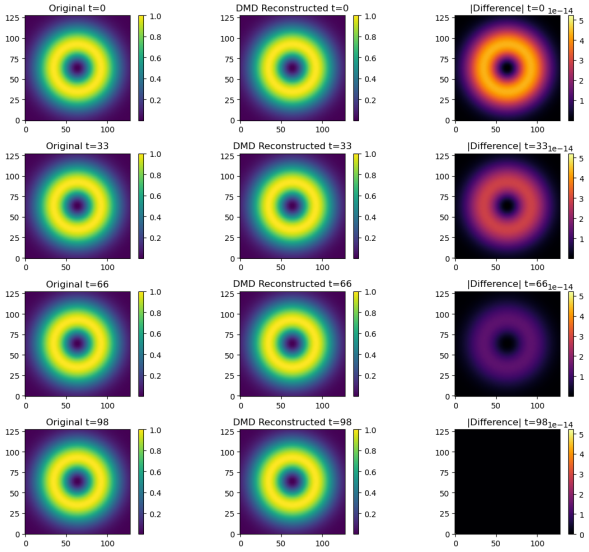

Figure 32: The DMD reconstruction of the 2D time-evolution of the magnon density; the index in the x and y directions represent the number of pixels used to represent the momentum space k_x and k_y respectively (48px). The simulation is ran for 10'000 timesteps. The difference column shows a complete match between the original data and the reconstruction (notice the scale of the difference)

5.5.2 Second reconstruction with duration=10000

The second simulation has a total duration of 10'000 time steps. The momentum space resolution is lower with 48x48 pixels.

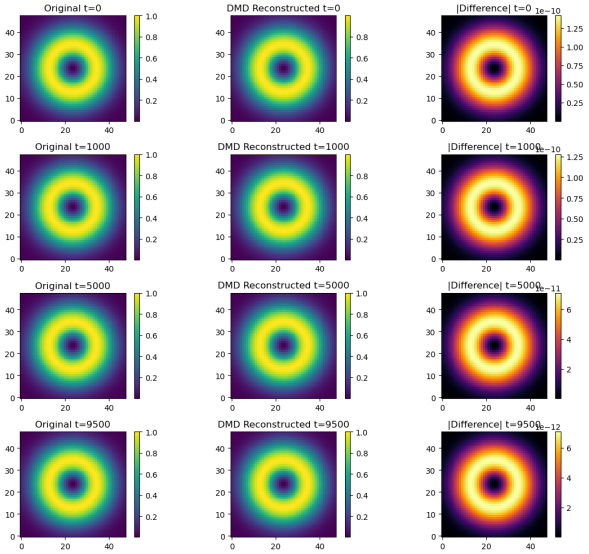

Figure 33: The DMD reconstruction of the 2D time-evolution of the magnon density; the index in the x and y directions represent the number of pixels used to represent the momentum space k_x and k_y respectively (128px). The simulation is ran for 100 timesteps. The difference column shows a complete match between the original data and the reconstruction (notice the scale of the difference)

5.5.3 Comparison of the value of the different singular values

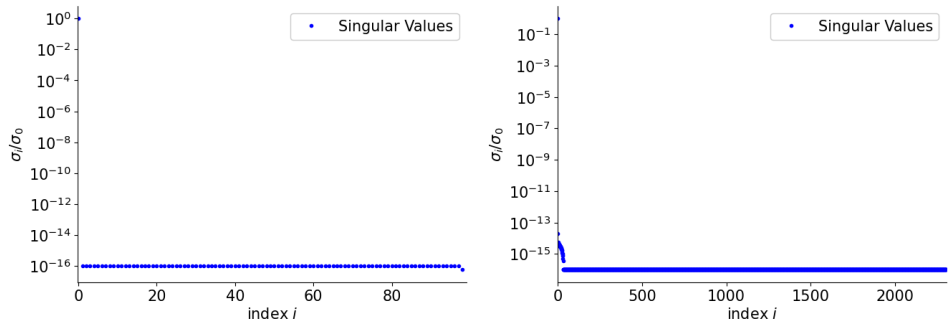

Figure 34: On the left, the singular values as a function of the index for the short duration simulation. On the right, the same plotting of the singular values but for the longer duration simulation.

6 Discussion

6.1 Simulation of density matrix

Overall, the simulation of the elements of the density matrix goes well. Use is made of the dynamics laid down in subsection 3.4. The results are expected to be coherent and accurate, given that the physics is well understood and relatively straightforward (See Appendix A for all 18 pulse-band structure simulations).

6.1.1 Off-diagonal elements of the density matrix

Figure 9 and 10 paint a clear picture of the effect of the different laser pulses on the coherence elements of the density matrix.
Interestingly, an important difference can be seen to emerge in the evolution of the coherence after the end of the different types of pulses.
In the case of the gaussian pulses (Figures 9), the coherence follows the excitation and goes back to zero after the latter settles down.
This is not always the case with the envelope pulse excitations (Figures 10), however. For the band structure 1, the coherence also follows the amplitude of the excitation. For the other band structures, on the other hand, the coherence remains in a steady oscillating state after the pulse disappears.
The decoherence occurs in the case of the band structure 1, the one with the widest band gap Δ of all three band structures. The ensuing impact on the amplitude of the change due to the electric pulse can also be seen in the valence and conduction bands. None-the-less, this non-trivial phenomenon only occurs in the off-diagonal elements of the density matrix.
Furthermore, it is to be noted that the amplitude of the envelope excitations are smaller than the amplitude of the simple gaussian pulses ($E_0 = 0.3, 0.7, 1.0$eV against $E_0 = 1.2, 1.7, 1.9$ eV). Consequently, it seems that the creation of a steady coherent state doesn't only require a stronger pulse or shallower band gap, but also an oscillating electric pulse.

6.1.2 The valence and conduction bands

As for the case of the off-diagonal elements of the density matrix, the corresponding graphs (Figures 11 and 12) also paint a clear picture of the effect of the different laser pulses on the population of the valence and conduction bands.
It clearly emerges that the increase in the population of the conduction band corresponds to the decrease in the population of the valence band, as should be expected.
Contrary to the off-diagonal elements, the population of the valence and conduction bands behave in a very similar way across all types and amplitudes of pulses and band structures.
In each case, after the laser pulse excitation, the population remains in an excited state.

6.2 Applying DMD to the density matrix

6.2.1 Failure of the basic DMD algorithm

As hinted at in subsection 2.3, DMD can be very weak when trying to pick up transient behaviors, or simple standing waves. As we have seen above, the effect of the electric pulse is very time-localized, which makes it difficult for simple DMD to detect. Figures 13 and 14 make it clear that simple DMD completely fails when trying to capture the modes of the off-diagonal elements of the density matrix. The same can be seen in figures 19, 20 and 21, for the reconstruction of the population of the two bands.

6.2.2 Hankel preprocessing

Applying Hankel preprocessing to the data matrices leads to much better results. For both the off-diagonal and diagonal elements, the DMD algorithm now yields excellent results.
Importantly, Hankel preprocessing must be relatively extensive in order to yield significant improvement. Settling for a total delay of 400 (out of a total of a 1000 steps) leads to an equal time-shortening of the reconstruction, even though it produces a very good match with the original data. This is an

important drawback.
Also, the matrices resulting from the preprocessing become significantly heavier to handle, which leads to a significant slowdown (and equivalent loss in efficiency) of the algorithm.
Interestingly, since the basic DMD algorithm leads to very bad results, the key determining factor in using Hankel preprocessed DMD in this specific case becomes the corresponding time delay -rather than the usual truncation rank. Figure 30 makes that shift very clear. The very limited effect of truncation rank on runtime (and consequently algorithmic efficiency) can be seen in Figure 31 and 29.

6.3 DMD on the magnon simulation

DMD applied to the magnon simulation yields very good results, even when using the basic version of the algorithm. This is in very stark contrast with the results obtained with the density matrix simulation.
A likely reason for the success of the algorithm in that context is the very slow evolution of the system over time. No strong effect appears in the time evolution of the magnon distribution, making it a much better candidate for applying the basic DMD algorithm.
Interestingly, the singular values decomposition reflects the fact that the magnon simulation is a good candidate for DMD. The two graphs in Figure 34 both display a single dominant mode. The other modes fall to values orders of magnitudes smaller than the small modes (around 10^{-16}) in the semiconductor simulation (usually around 10^{-6} - 10^{-7}). Furthermore, the longer simulation can be seen to introduce a few more mode (although very small), which is coherent with its much longer duration.

Acknowledgments

I would like to thank Dr. Michael Schüler for providing me with the opportunity to work on this topic and guiding me along the way. I would also like to thank Juan Felipe Pulgarin Mosquera for his help and support in the project.

References

[1] *Gauge Invariance of Light-Matter Interactions in First-Principle Tight-Binding Models*, Michael Schüler, Jacob A. Marks, Yuta Murakami, Chunjing Jia, and Thomas P. Devereaux, 2021

[2] *Fundamentals of Semiconductors: Physics and Materials Properties*, P. Y. Yu and M. Cardona, 4th ed., Springer, 2010

[3] *Quantum Theory of the Optical and Electronic Properties of Semiconductors*, H. Haug and S. W. Koch, 4th ed., World Scientific, 2004

[4] *A Short Course on Topological Insulators: Band-structure topology and edge states in one and two dimensions*, Asbóth, J. K., Oroszlány, L., and Pályi, A., 2015

[5] *Semiconductors I: Band Theory I*, Weatherill, D., lecture notes. `https://indico.global/event/1768/contributions/30811/attachments/15756/25185/semiconductors1.pdf`

[6] *Wigner-Seitz cell, wikipedia*, `https://en.wikipedia.org/wiki/Wigner%E2%80%93Seitz_cell`

[7] *Physics of Semiconductor Devices, Third Edition, S. M. Sze and Kwok K. Ng*

[8] *MIT OpenCourseWare: Fundamentals of Photonics, Chapter 6: Interaction of Light and Matter*, MIT OCW

[9] *Fundamentals of Magnonics, Sergio M. Rezende*, Lecture Notes in Physics, Vol. 969, Springer, 2020, `https://doi.org/10.1007/978-3-030-41317-0`.

[10] *Field Dependence of the Intrinsic Domain Magnetization of a Ferromagnet, Hallstein and Prikamoff*,

[11] *Nonequilibrium phase transition in a driven-dissipative quantum antiferromagnet*, M. H. Kalthoff, D. M. Kennes, A. J. Millis, and M. A. Sentef, Phys. Rev. Research, vol. 4, 023115, 2022.

[12] *Dynamic Mode Decomposition: Data-Driven Modeling of Complex Systems, Kutz, Brunton, Brunton, and Proctor*, .

[13] *Compressive sampling and dynamic mode decomposition*, Brunton, Proctor and Kutz, 2013

[14] *Dynamic Mode Decomposition with Control*, Proctor, J. L., Brunton, S. L., and Kutz, J. N., 2014

[15] *Forecasting Long-Time Dynamics in Quantum Many-Body Systems by Dynamic Mode Decomposition*, Kaneko, R., Imada, M., Kabashima, Y., and Ohtsuki, T., 2024

[16] *Using Dynamic Model Decomposition to Predict the Dynamics of a Two-time Non-equilibrium Green's function*, Yin et al. 2022

[17] *A fast and accurate basis pursuit denoising algorithm with application to super-resolving tomographic SAR*, Shi et al. 2018

[18] *NumPy – Harris, Millman, van der Walt et al.*, Nature 585, 357–362 (2020), `https://doi.org/10.1038/s41586-020-2649-2`

[19] *SciPy – Virtanen, Gommers, Oliphant et al.*, Nature Methods 17, 261–272 (2020), `https://doi.org/10.1038/s41592-019-0686-2`

[20] *Matplotlib – Hunter, J.D.*, Computing in Science & Engineering, 9(3), 90–95 (2007), `https://doi.org/10.1109/MCSE.2007.55`

[21] *PyDMD - Python Dynamic Mode Decomposition, Demo and Tezzele*, `https://github.com/PyDMD`.

7 Appendix A: More on the time evolution of the density matrix

In this Appendix, we list the effect of all six pulses (3 gaussian, 3 envelope) on each of the three band structures.

Effects on the off-diagonal elements

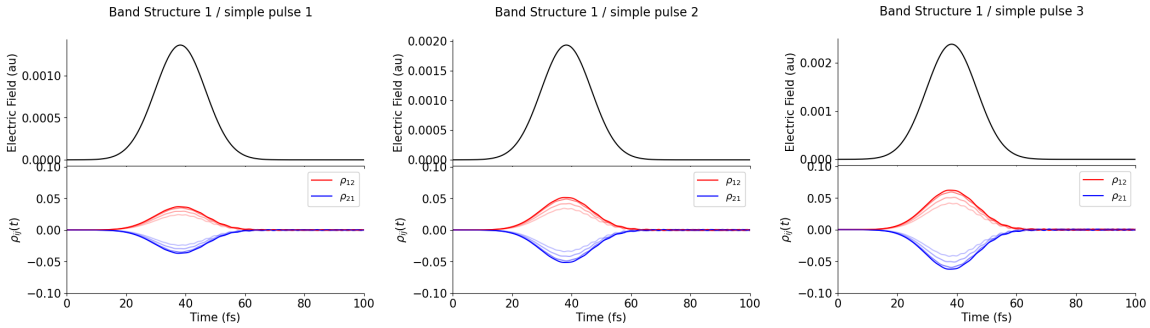

Figure 35: Effect of all three simple pulses on the first ($J = 0.5$, $\Delta = 1.0$) band structure

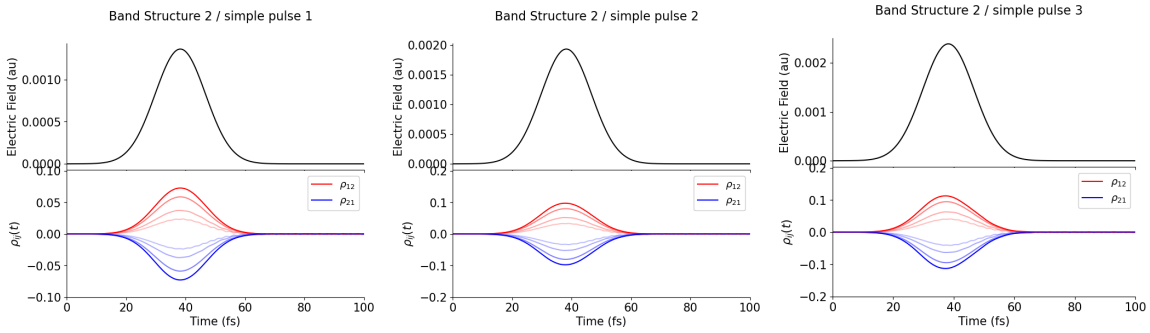

Figure 36: Effect of all three simple pulses on the second ($J = 1.0$, $\Delta = 0.5$) band structure

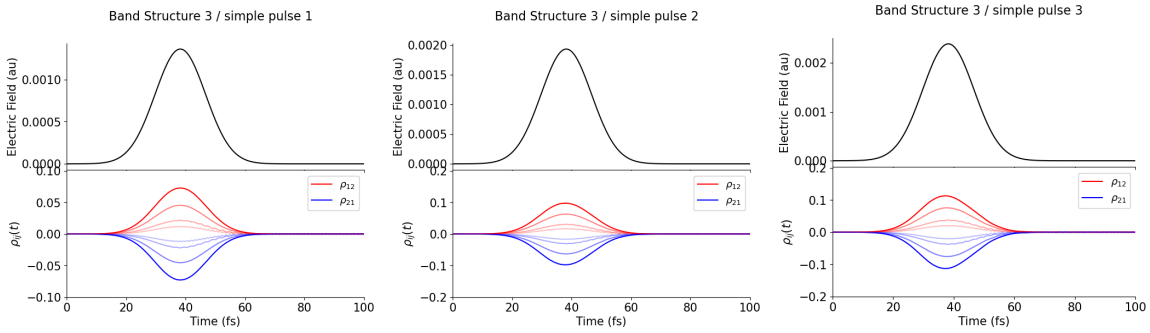

Figure 37: Effect of all three simple pulses on the first ($J = 2.5$, $\Delta = 0.5$) band structure

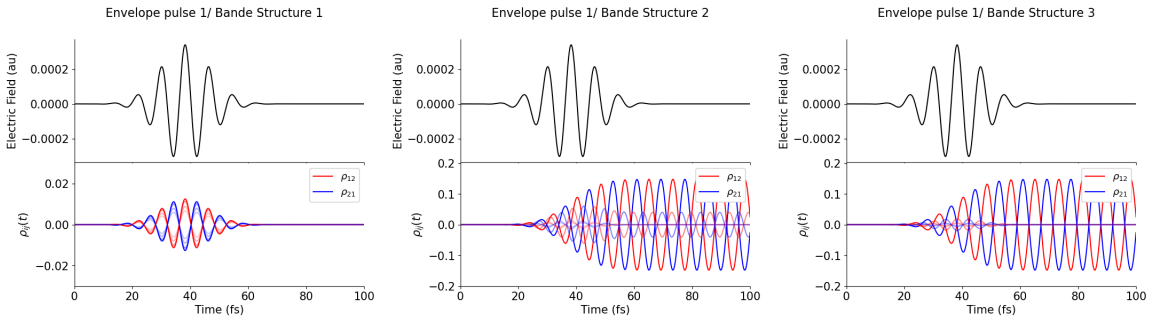

Figure 38: Effect of the envelope pulse with $E_0 = 0.3$ on all three band structures

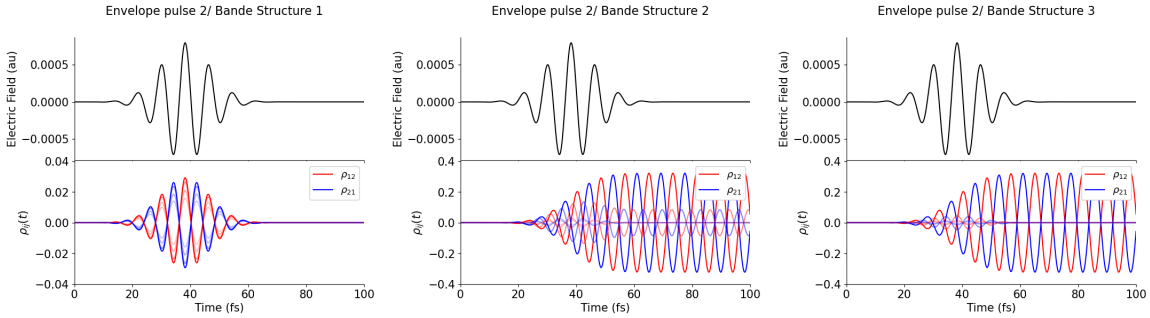

Figure 39: Effect of the envelope pulse with $E_0 = 0.7$ on all three band structures

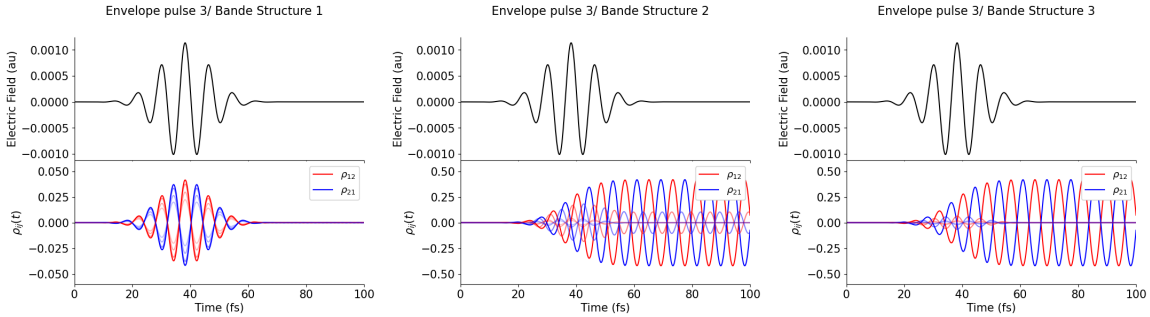

Figure 40: Effect of the envelope pulse with $E_0 = 1.0$ on all three band structures

Effects on the diagonal elements

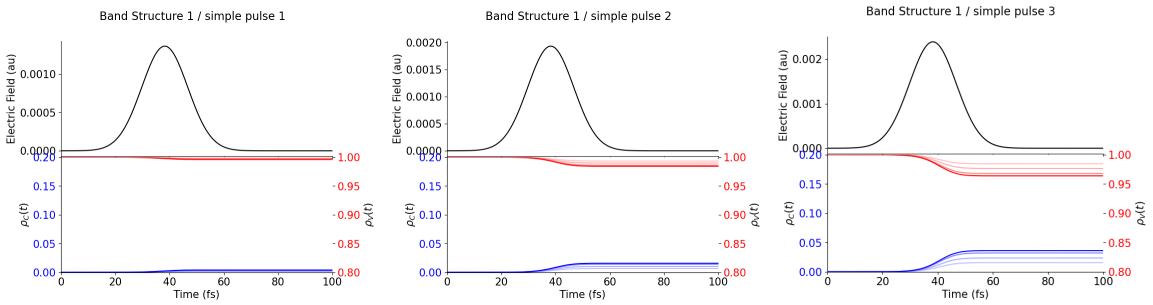

Figure 41: Effect of all three simple pulses on the first ($J = 0.5$, $\Delta = 1.0$) band structure

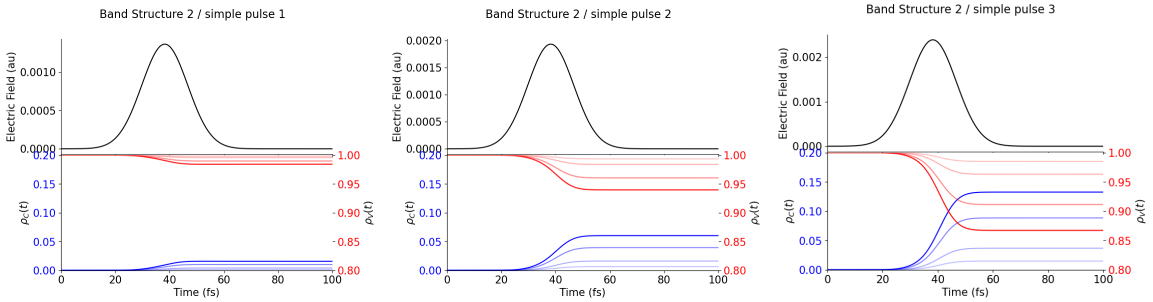

Figure 42: Effect of all three simple pulses on the second ($J = 1.0$, $\Delta = 0.5$) band structure

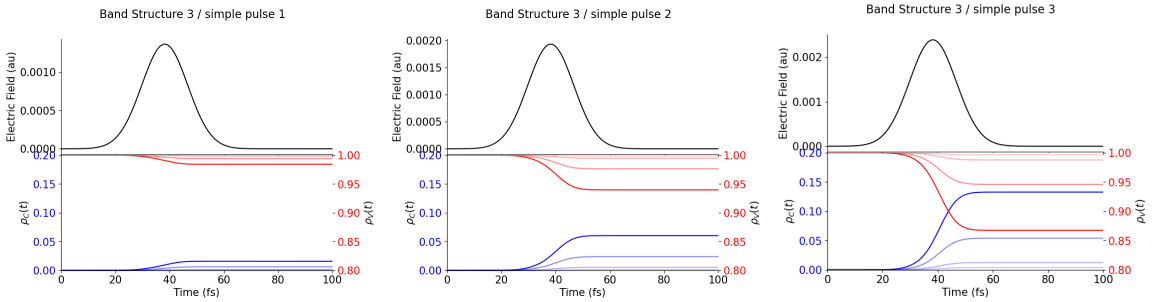

Figure 43: Effect of all three simple pulses on the first ($J = 2.5$, $\Delta = 0.5$) band structure

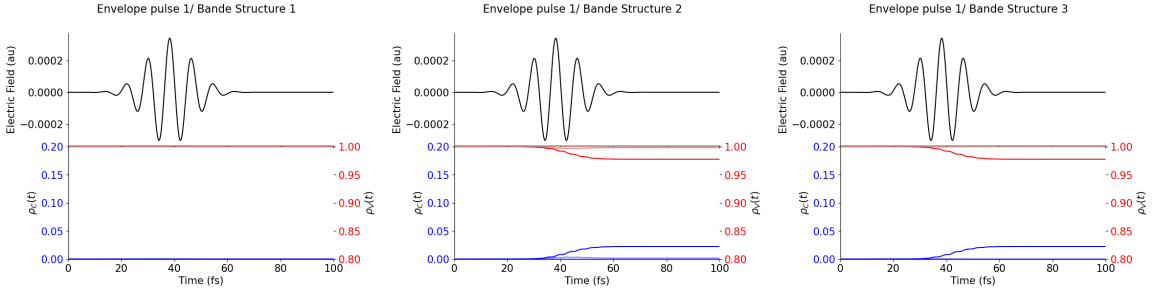

Figure 44: Effect of the envelope pulse with $E_0 = 0.3$ on all three band structures

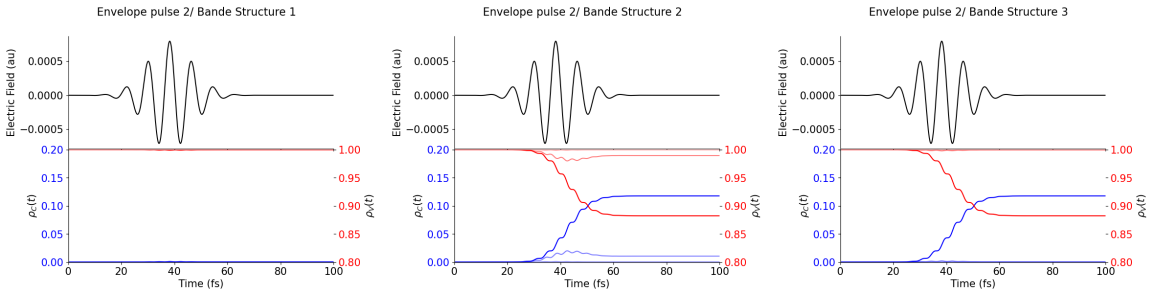

Figure 45: Effect of the envelope pulse with $E_0 = 0.7$ on all three band structures

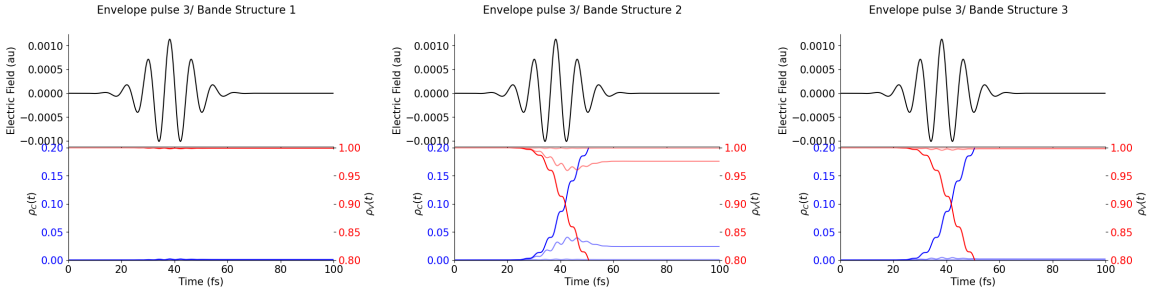

Figure 46: Effect of the envelope pulse with $E_0 = 1.0$ on all three band structures